

Early r -process Enrichment and Hierarchical Assembly Across the Sagittarius Dwarf Galaxy*

XIAOWEI OU ^{1,2} ALEXANDER YELLAND ^{1,2} ANIRUDH CHITI ^{3,4} ANNA FREBEL ^{1,2} GUILHERME LIMBERG ^{3,4} AND
MOHAMMAD K. MARDINI ^{2,5,6,7}

¹MIT Department of Physics, 77 Massachusetts Avenue, Cambridge, MA 02139, USA

²MIT Kavli Institute for Astrophysics and Space Research, 77 Massachusetts Avenue, Cambridge, MA 02139, USA

³Department of Astronomy & Astrophysics, University of Chicago, 5640 S. Ellis Avenue, Chicago, IL 60637, USA

⁴Kavli Institute for Cosmological Physics, University of Chicago, Chicago, IL 60637, USA

⁵Department of Physics, Zarqa University, Zarqa 13110, Jordan

⁶Jordanian Astronomical Virtual Observatory, Zarqa University, Zarqa 13110, Jordan

⁷Joint Institute for Nuclear Astrophysics – Center for the Evolution of the Elements (JINA-CEE), USA

ABSTRACT

Dwarf galaxies like Sagittarius (Sgr) provide a unique window into the early stages of galactic chemical evolution, particularly through their metal-poor stars. By studying the chemical abundances of stars in the Sgr core and tidal streams, we can gain insights into the assembly history of this galaxy and its early heavy element nucleosynthesis processes. We efficiently selected extremely metal-poor candidates in the core and streams for high-resolution spectroscopic analysis using metallicity-sensitive photometry from SkyMapper DR2, and *Gaia* DR3 XP spectra and proper motions. We present a sample of 37 Sgr stars with detailed chemical abundances, of which we identify 10 extremely metal-poor (EMP; $[\text{Fe}/\text{H}] \leq -3.0$) stars, 25 very metal-poor (VMP; $[\text{Fe}/\text{H}] \leq -2.0$) stars, and 2 metal-poor (MP; $[\text{Fe}/\text{H}] \leq -1.0$) stars. This sample increases the number of extremely metal-poor Sgr stars analyzed with high-resolution spectroscopy by a factor of five. Of these stars, 15 are identified as members of the Sgr tidal stream, while the remaining 22 are associated with the core. We derive abundances for up to 20 elements and identify no statistically significant differences between the element abundance patterns across the core and stream samples. Intriguingly, we identify stars that may have formed in ultra-faint dwarf galaxies that accreted onto Sgr, in addition to patterns of C and r -process elements distinct from the Milky Way halo. Over half of the sample shows a neutron-capture element abundance pattern consistent with the scaled solar pure r -process pattern, indicating early r -process enrichment in the Sgr progenitor.

Keywords: Galaxy stellar content (621) — Chemical enrichment (225) — Sagittarius dwarf spheroidal galaxy (1423) — Stellar abundances (1577) — Galactic archaeology (2178) — Galaxy chemical evolution (580)

1. INTRODUCTION

Understanding the chemical evolution of galaxies is fundamental for analyzing how elements are synthesized and distributed over cosmic timescales (see e.g., Burbidge et al. 1957; Timmes et al. 1995; Beers & Christlieb 2005; Nomoto et al. 2013; Maiolino & Mannucci 2019; Kobayashi et al. 2020). Through cycles of star formation and stellar nucleosynthesis in a galaxy, its stars, supernovae, and compact remnants enrich the interstellar medium with heavier elements (see e.g., Chiappini et al. 1997; Tacconi et al. 2020). Each new generation of stars forms with the chemical composition of their

surrounding gas. Therefore, ancient, metal-poor stars serve as unique probes of the early stages of galactic chemical enrichment (see e.g., Beers & Christlieb 2005; Frebel & Norris 2015). By examining the chemical compositions of metal-poor stars in the Milky Way’s satellite dwarf galaxies, we can learn about the evolution, assembly history, and early chemical enrichment of small-scale systems (see e.g., Tolstoy et al. 2009; Kirby et al. 2013; Helmi 2020; Deason & Belokurov 2024).

Dwarf galaxies exhibit a wide range of physical properties, including total stellar mass, star formation histories, and environmental interactions (McConnachie 2012; Pace 2024). Consequently, the chemical evolution of these systems is strongly influenced by the varying rates of star formation, metal mixing, and the frequency of enrichment events such as supernovae, neutron star

* This paper includes data gathered with the 6.5 meter Magellan Telescopes located at Las Campanas Observatory, Chile.

mergers, or asymptotic giant branch (AGB) star contributions (Tolstoy et al. 2009). Recent studies have begun to focus on the evolution of neutron-capture elements as they can provide specific details about the formation history and early star formation (Cohen & Huang 2009; Skúladóttir et al. 2019; Skúladóttir & Salvadori 2020; Hirai et al. 2024). In particular, europium abundances in low-metallicity stars were measured in disrupted dwarf systems (Matsuno et al. 2021; Naidu et al. 2022; Ernandes et al. 2024; Ou et al. 2024; Limberg et al. 2024; Atzberger et al. 2024) and globular clusters (Monty et al. 2024; Ceccarelli et al. 2024). Several of these measurements exhibited a clear rise in $[\text{Eu}/\text{Fe}]$ with increasing metallicity; a trend that has been attributed to a delayed r -process source, such as a neutron star merger, as the origin of europium (Naidu et al. 2022; Frebel & Ji 2023; Limberg et al. 2024; Ernandes et al. 2024; Ou et al. 2024). Similarly, the ultra-faint dwarf (UFD) Reticulum II shows strong r -process enhancement in the majority of its stars, also suggesting the operation of early neutron star mergers (see e.g., Ji et al. 2016). Nevertheless, the overall quantity of available europium measurements remains sparse in dwarf galaxies.

In this study, we focus on the Sagittarius (Sgr) dwarf galaxy and its associated stellar stream. Sgr is located near the inner Galactic region of the Milky Way and is currently disrupting (Ibata et al. 1994, 1995). The core of Sgr is located approximately ~ 25 kpc away (Ibata et al. 1997; Mateo 1998; Ferguson & Strigari 2020). However, over the past ~ 5 Gyr, Sgr has undergone significant tidal stripping due to its interactions with the Milky Way, resulting in the formation of two prominent stellar streams (Majewski et al. 2003), winding twice around the Milky Way and extending across the sky. Though it remains one of the Milky Way’s most massive dwarf galaxies, this ongoing tidal stripping of Sgr has torn a significant amount of stellar mass away from the core. Today, the stellar mass of Sgr is $\sim 10^8 M_\odot$ (Vasiliev & Belokurov 2020), whereas prior to tidal disruption, it is estimated to have been up to $\sim 10^{10} M_\odot$ (Niederste-Ostholt et al. 2010). Hence, Sgr provides a unique opportunity to investigate the erstwhile internal radial distribution of chemical enrichment process(es) in the early Sgr system and to use its present-day core and stream stars to reconstruct this complex evolutionary history.

Following a host of studies involving more metal-rich stars (e.g., Hasselquist et al. 2017; Hansen et al. 2018), the Pristine Inner Galaxy Survey (PIGS) (Sestito et al. 2024a,b; Vitali et al. 2024) collected medium to high-resolution spectra of the Sgr stars, including a sample of ten very metal-poor (VMP; $[\text{Fe}/\text{H}] \leq -2.0$) and two extremely metal-poor (EMP; $[\text{Fe}/\text{H}] \leq -3.0$) stars, to study the early chemical enrichment in the Sgr core. These studies have shown the importance of examining the earliest phases of chemical evolution in Sgr and its

specific nucleosynthesis event(s) to understand its assembly history.

Accordingly, we have collected a low-metallicity sample of stars in the Sgr core and stream to further investigate its early history. We obtain a sample of 37 Sgr stars and identify ten EMP stars, 25 VMP stars, and 2 metal-poor (MP; $[\text{Fe}/\text{H}] \leq -1.0$) stars, increasing the number of EMP stars with high-resolution spectroscopy observation by a factor of five. We find that at least half the stars in the sample, across both the core and the stream, contain r -process elements whose abundances agree with the scaled solar r -process pattern. This makes Sgr another “ r -process” galaxy that experienced one (or even multiple) prompt r -process events at early times, prior to the formation of its stellar populations with $-3.3 < [\text{Fe}/\text{H}] \lesssim -2$. This highlights that some dwarf galaxies appear to be widely enriched by r -process elements at early times, which so far has been limited to Reticulum II with possibly Tucana 3 (Hansen et al. 2017; Marshall et al. 2019) and Grus II (Hansen et al. 2020) due to their uncertain nature (Simon et al. 2017, 2020).

2. TARGET SELECTION AND OBSERVATIONS

To carry out an initial selection of the core member stars, we adopt the heliocentric Sgr coordinate system (Λ_\odot, B_\odot) from Majewski et al. (2003) and Law & Majewski (2010). The longitude, Λ_\odot , is centered on the Sgr core ($\Lambda_\odot = 0^\circ$) and increases in the direction of the trailing Sgr debris, whereas the latitude, B_\odot , is aligned with the debris midplane and positive toward the orbital pole ($l_{\text{GC}}, b_{\text{GC}} = (273.8^\circ, -13.5^\circ)$). We take the Sgr core to be located at Galactic coordinates $(l, b) = (5.6^\circ, -14.2^\circ)$ and Sgr coordinates $(\Lambda_\odot, B_\odot) = (0, 0)$ (Majewski et al. 2003). The core membership is then constrained to the stars within a few degrees of the core, as seen in Table 1.

We also used *Gaia* DR3 proper motions to constrain our initial target selection and ensure a high-purity sample of Sgr member stars in its core and stream. In the core of Sgr, we first selected stars with proper motions broadly consistent with its systemic value ($-3.6 \text{ mas yr}^{-1} < \mu_\alpha < -2.7 \text{ mas yr}^{-1}$ and $-1.6 \text{ mas yr}^{-1} < \mu_\delta < -1.2 \text{ mas yr}^{-1}$), as in Chiti et al. (2020b). Along its stream, we first selected stars based solely on proper motion criteria presented in Ramos et al. (2022), which identified and described the proper motion trends along the Sgr tidal streams.

Of our target selection, our metal-poor candidates in the Sagittarius (Sgr) dwarf galaxy were selected using metallicity-sensitive photometry from SkyMapper DR2 (Onken et al. 2019) and synthetic photometry derived from *Gaia* XP spectra (Gaia Collaboration et al. 2016, 2021, 2023). For targets observed before 2023, we used photometric metallicities derived from SkyMapper DR2 in Chiti et al. (2021) to select candidates in the core of Sgr. Five low metallicity stars were observed in this manner (see Table 1), but a number of original can-

didates ended up being contaminants with unresolved line-of-sight companions due to high median seeing at the SkyMapper site (Onken et al. 2019). With *Gaia* DR3, we circumvented this issue by performing target selection using the flux-calibrated BP/RP spectra (also known as XP spectra; Carrasco et al. 2021; De Angeli et al. 2023) and excluding stars that had companions within $2''0$ based on *Gaia* astrometry. This XP-based target selection was performed by generating synthetic SkyMapper v, g, i and narrow-band Ca H&K photometry through the Pristine survey passband (Starkenburger et al. 2017a; analogous to Martin et al. 2024) using the GaiaXPpy toolkit¹ (Gaia Collaboration et al. 2023). We then derived photometric metallicities following the methods in Chiti et al. (2020c); our metallicities for the XP catalog have demonstrably been used to identify the lowest metallicity stars, e.g., in the LMC (Chiti et al. 2024) and also led to the discovery of an ultra metal-poor star in the Milky Way disk (Mardini et al. 2024). Combining the coordinate, proper motion, and photometric metallicity selections resulted in a sample of ~ 200 stars in the Sgr core and stream.

We then obtained follow-up high-resolution spectroscopy of ~ 20 stars in the stream and ~ 40 stars in the core using the Magellan Clay 6.5 m Telescopes at Las Campanas Observatory using the Magellan Inamori Kyocera Echelle (MIKE) spectrograph (Bernstein et al. 2003) in 2021 July and 2023 May and June. All stars were observed with the $1''0$ slit and 2×2 binning, yielding a resolving power of $R \sim 28,000/22,000$ on the blue/red arm of MIKE with wavelength coverage 3200–5000 and 4900–10000 Å, respectively. The spectra were reduced with the Carnegie Python pipeline (Kelson 2003). After shifting the spectra to rest, individual orders were normalized and stitched together into a final spectrum before analysis. Table 1 lists the coordinates for our observed targets, dates of their observation, exposure time, magnitudes, radial velocities, and signal-to-noise (S/N) ratios per pixel at 4500 and 6500 Å.

We derived radial velocities for these stars by cross-correlating their spectra against a template spectrum of HD122563. During data collection, to avoid observing interlopers (non-member candidates beyond a first snapshot exposure), we performed on-the-fly checks on the radial velocity and metallicity via visual inspection of the reduced exposures. Accordingly, stars with spuriously high metallicities (often resulting from the existence of unresolved companions, as discussed above) or radial velocities incongruent with membership were promptly excluded from further observations from the sample (about 20 stars). The final sample consists of 37 stars.

For final confirmation of Sgr membership in the sample, we used radial velocities obtained from the total

exposures and distance estimates from the Bayesian isochrone-fitting code StarHorse (Santiago et al. 2016; Queiroz et al. 2018) to complete the 6D kinematics. In the Sgr core, we broadly confirm that our stars have radial velocities in the range 100–180 km s⁻¹ (Ibata et al. 1994; Bellazzini et al. 2008). To confirm stream membership, we used the procedure in Limberg et al. (2023) that computes actions and angular momenta of the stars based on the 6D phase-space coordinates. Based on the computed actions and angular momenta of the stars, as shown in Figure 2 of Limberg et al. (2023), all our stream candidates are confirmed. Since all 37 stars meet the respective criteria, our final sample consists of 22 stars with kinematics consistent with that of the core of Sgr, and 15 stars have properties in agreement with the kinematic signature of the tidal streams.

3. STELLAR PARAMETERS AND CHEMICAL ABUNDANCE ANALYSIS

3.1. Photometric stellar parameters

To find our first estimate of the stellar parameters (T_{eff} , $\log g$, $[\text{Fe}/\text{H}]$, v_t) and to reaffirm that these stars are not foreground contamination, we begin by determining them spectroscopically. For this analysis, we used ATLAS model atmospheres from Castelli & Kurucz (2003), with α enhancement, as described further in Section 3.2. We obtained the effective temperatures (T_{eff}) by requiring no trend in the Fe I measurements as a function of excitation potential energy. Surface gravities ($\log g$) were derived by enforcing ionization balance between Fe I and Fe II lines. Metallicities ($[\text{Fe}/\text{H}]$) were set based on the average of all available Fe I lines measured. Microturbulences (v_t) were set by requiring that Fe I have no trend with reduced equivalent width (REW). The process was iterated until convergence. In the end, no stars were found to have $\log g$ inconsistent with being a luminous, distant red giant, further affirming their membership to Sgr.

This spectroscopic approach of deriving stellar parameters, however, typically produces cooler T_{eff} and lower $\log g$ compared to photometric methods for cool, metal-poor stars due to non-local thermodynamic equilibrium (NLTE) effects in Fe I (e.g., Frebel et al. 2013; Ezzeddine et al. 2017). Using these spectroscopically derived $[\text{Fe}/\text{H}]$ and v_t as initial guesses, we thus proceed to determine our photometric stellar parameters. Photometric T_{eff} was derived by using *Gaia* DR3 $G - RP$ colors (Gaia Collaboration et al. 2021) with color- $[\text{Fe}/\text{H}] - T_{\text{eff}}$ relations from Mucciarelli et al. (2021). We retrieved photometry data from the *Gaia* DR3 archive for the target stars and calculated the unextincted magnitudes

¹ <https://gaia-dpci.github.io/GaiaXPpy-website/>

Table 1. Observational Parameters.

Star name	<i>Gaia</i> DR3 Designation	R.A.	Decl.	Λ_{\odot}	B_{\odot}	UT Date	t_{exp}	g	v_{helio}	S/N
		(h:m:s)	(d:m:s)	(deg)	(deg)		(s)	(mag)	(km s $^{-1}$)	
Stream										
○ Sgr421	620763790933951488	09:36:00.0	+17:07:21.4	216.9	11.6	2023 May 24	1320	14.5	140.1	32, 63
○ Sgr422	626434144197068160	09:57:30.0	+18:30:17.4	221.7	9.2	2023 May 25	4163	16.2	−61.8	13, 23
○ Sgr423	722010223233565952	10:21:32.3	+21:46:38.8	226.4	4.6	2023 May 24	2100	15.0	−42.8	32, 62
○ Sgr424	720678611573056384	10:28:03.8	+20:16:15.9	228.3	5.7	2023 May 25	1500	15.4	−41.7	22, 41
○ Sgr426	3987367858589682432	10:35:36.8	+20:33:51.4	229.9	4.9	2023 May 25	2100	15.1	−51.8	31, 62
○ Sgr428	3897736907644138368	11:49:36.0	+06:15:31.9	252.0	11.8	2023 May 25	1200	15.9	193.4	19, 35
○ Sgr430	3918753557013284608	12:05:57.8	+11:26:28.1	253.5	5.4	2023 May 25	2106	14.7	−18.3	35, 82
○ Sgr431	3707325064494295552	12:36:03.1	+04:22:23.4	263.4	8.3	2023 Jun 25	4794	16.1	9.8	18, 40
○ Sgr434	3708871630677912320	12:48:19.6	+05:44:47.2	265.5	5.7	2023 Jun 25	2754	15.7	−8.5	24, 43
○ Sgr438	3742595885684658560	13:17:16.3	+12:51:15.1	268.3	−4.0	2023 May 26	3990	15.8	−103.0	28, 47
○ Sgr441	3726554388991980800	13:38:16.5	+10:54:19.8	273.8	−4.8	2023 May 26	5999	15.4	−22.1	20, 51
○ Sgr442	3713742742066109568	13:39:13.6	+04:20:10.8	277.3	0.7	2023 May 25	1800	15.2	123.2	29, 57
○ Sgr449	3724011729697503616	14:02:29.1	+10:17:36.9	279.2	−7.3	2023 May 25	1537	14.7	−140.2	36, 66
○ Sgr452	3654980335256551808	14:34:27.4	+00:57:43.5	290.9	−3.3	2023 May 25	3386	16.2	−7.3	24, 51
○ Sgr453	4415617329687172224	15:20:10.2	−00:55:16.2	301.8	−7.4	2023 Jun 26	1500	15.1	−216.7	17, 41
Core										
● Sgr459	4046752756534194304	18:35:35.3	−31:04:52.3	356.0	2.9	2023 Jun 26	2400	15.1	170.3	23, 53
● Sgr460	4046692626988248704	18:37:37.0	−31:12:18.7	356.5	2.9	2023 May 25	3378	15.9	154.7	26, 54
● Sgr462	4047106558751402112	18:39:44.8	−30:37:02.0	356.8	2.3	2023 May 26	3600	15.8	157.4	29, 61
● Sgr463	4047227809930988288	18:43:10.7	−30:13:29.2	357.5	1.7	2023 May 26	4435	15.0	161.7	31, 71
● Sgr468	6732306574448077824	18:49:32.1	−34:35:45.8	359.6	5.8	2023 May 26	3964	15.3	135.3	30, 68
● Sgr2	6735720523692986368	18:49:59.0	−33:49:51.5	359.6	5.0	2021 Jul 30	2673	15.3	171.9	24, 57
● Sgr471	6736253885603451776	18:50:53.7	−31:33:17.7	359.3	2.7	2023 Jun 26	3000	15.1	148.0	28, 61
● Sgr476	6736183692971769472	18:52:10.3	−31:54:13.2	359.7	3.0	2023 May 26	4307	14.9	166.1	29, 72
● Sgr69	6761301211485896192	18:52:48.5	−29:32:23.4	359.4	0.7	2021 Jul 31	600	15.1	136.8	9, 26
● Sgr482	6760843501083241216	18:56:40.2	−29:54:02.0	0.3	0.9	2023 May 25	2135	15.3	147.1	28, 58
● Sgr4	6760823641153762816	18:57:04.5	−30:10:21.6	0.4	1.1	2021 Jul 30	1200	14.9	140.3	17, 47
● Sgr38	6760148545331944832	18:57:27.7	−31:07:39.9	0.6	2.0	2021 Jul 31	3225	16.0	162.2	19, 45
● Sgr484	6756665051965670400	19:01:38.9	−32:54:27.2	1.8	3.7	2023 May 25	3175	15.8	159.0	27, 55
● Sgr488	6755741496554745728	19:05:13.1	−34:09:16.6	2.7	4.8	2023 May 26	2833	15.2	139.6	25, 57
● Sgr492	6757188660021199360	19:06:12.1	−31:55:04.5	2.6	2.5	2023 May 26	1200	15.2	143.7	10, 25
● Sgr495	6757333348879294336	19:09:05.2	−31:06:32.8	3.1	1.6	2023 May 25	1506	14.7	157.6	29, 67
● Sgr496	6762312242461355008	19:10:57.1	−28:53:15.9	3.2	−0.6	2023 May 25	2602	15.7	120.6	25, 55
● Sgr9	6756198442417269504	19:14:03.2	−32:42:03.5	4.4	3.1	2021 Jul 30	2400	15.5	122.3	20, 50
● Sgr504	6756126841019510784	19:14:48.7	−33:07:52.9	4.6	3.5	2023 Jun 26	1500	15.2	148.1	24, 47
● Sgr505	6759005362463205760	19:15:12.0	−29:53:26.1	4.2	0.3	2023 Jun 26	3000	15.3	136.0	22, 47
● Sgr509	6744030735644086784	19:18:30.2	−33:42:59.7	5.4	4.0	2023 May 25	2892	15.7	169.9	30, 59
● Sgr512	6744069390349796224	19:19:57.4	−33:13:50.9	5.7	3.4	2023 May 25	2110	15.4	121.5	26, 55

Stars found in the Sagittarius core are denoted with black-filled circles (●), and stars found the Sagittarius streams are denoted with white-filled circles (○). Signal-to-noise (S/N) per pixel is listed for 4500 Å and 6500 Å.

using the extinction law provided by *Gaia*² and the extinction map from (Schlafly & Finkbeiner 2011).

For our final $\log g$, we opted to use the isochrone fitting method rather than calculating directly from the distances. The latter requires stars to have well-measured parallaxes (e.g., Ji et al. 2020). Because most of the Sgr stars are at distances beyond the resolution limit for *Gaia* parallax measurements, the astrometric distances tend to be underestimated, resulting in over-estimated $\log g$. We used low-metallicity Dartmouth

isochrones of the red giant branch (Dotter et al. 2008) to obtain the corresponding $\log g$ for all our sample stars. For the few stars with $[\text{Fe}/\text{H}] > -2.5$, we simply interpolate the Dartmouth isochrones in accordance to the metallicity to obtain their $\log g$. However, the majority of the stars have $[\text{Fe}/\text{H}] < -2.5$, which is below the $[\text{Fe}/\text{H}]$ grid limit of $[\text{Fe}/\text{H}] = -2.5$ of the isochrones. Hence, we adopt the $[\text{Fe}/\text{H}] = -2.5$ isochrone for these stars, knowing that the lower metallicity isochrones asymptotically converge, as shown in Figure 1. In addition, nine stars have photometric $T_{\text{eff}} \lesssim 4500$ K, making them too cool to fit on the computed isochrones. We thus extrapolate the isochrone tracks by 150 k to lower

² <https://www.cosmos.esa.int/web/gaia/edr3-extinction-law>

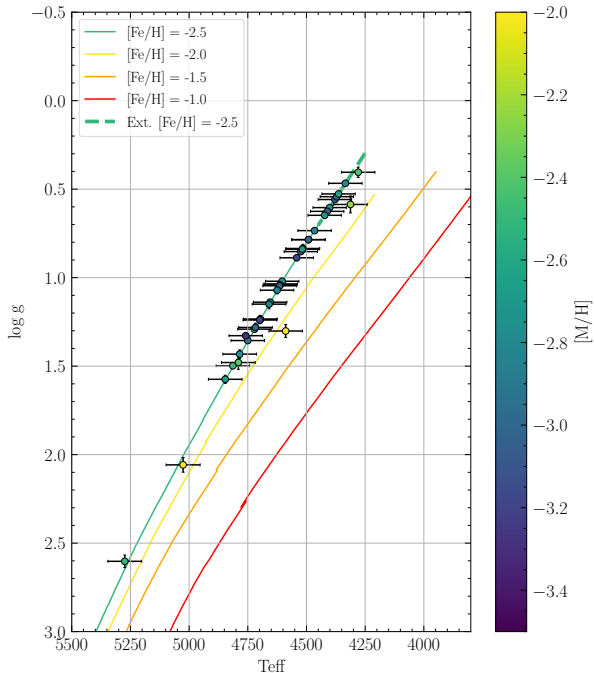


Figure 1. Kiel diagram for the sample with all stars shown in dots. The Dartmouth isochrones are shown in solid lines. The dashed line represents the extrapolated isochrone. Both the stars and isochrones are color-coded by metallicity.

T_{eff} , assuming that the isochrone behaves qualitatively linearly towards the tip of the red giant branch.

After obtaining final values for the surface gravity and the effective temperature, we then re-determined v_t and $[\text{Fe}/\text{H}]$ from Fe I. We further iterated these calculations, given that all stellar parameters depend on $[\text{Fe}/\text{H}]$.

Statistical uncertainties on T_{eff} and $\log g$ were determined by propagating input uncertainties (i.e., the *Gaia* photometry and $[\text{Fe}/\text{H}]$ uncertainties) through the color- $[\text{Fe}/\text{H}]-T_{\text{eff}}$ relations and isochrone fitting, respectively. The v_t statistical uncertainty was determined from the 1- σ confidence interval in the fitted slope with respect to REW. Typical statistical uncertainties are ~ 72 K for T_{eff} (dominated by uncertainties in $[\text{Fe}/\text{H}]$), ~ 0.02 dex for $\log g$, and ~ 0.25 dex for v_t .

Systematic uncertainties on T_{eff} and $\log g$ arise from choices in the color- $[\text{Fe}/\text{H}]-T_{\text{eff}}$ relations and isochrones. Specifically, these relations are computed assuming certain stellar evolution and spectral energy distribution models. The v_t is derived from the measured Fe lines and is thus susceptible to systematic uncertainties originating from the assumed 1D LTE stellar atmosphere models. Consequently, we adopt systematic uncertainties of 100 K, 0.2 dex, and 0.2 km s^{-1} for T_{eff} , $\log g$, and

v_t , respectively, which generally reflect these systematic analysis choices (Frebel et al. 2013).

To arrive at our total uncertainties, we add the systematic uncertainties in quadrature to the statistical uncertainties. For all stars, we find the typical total uncertainties in T_{eff} , $\log g$, and v_t to be ~ 122 K, ~ 0.20 dex, and $\pm 0.30 \text{ km s}^{-1}$, respectively.

The final stellar parameters and associated uncertainties are shown in Table 2. The reported $[\text{Fe}/\text{H}]$ and its associated uncertainties are computed based on the total uncertainties of T_{eff} , $\log g$, and v_t . Specifically, the uncertainties in stellar parameters introduce uncertainties in the derived element abundances. We propagate these uncertainties through the element abundances, including $[\text{Fe}/\text{H}]$, calculation following the procedure described in Section 3.2.

3.2. Element abundance determination

We now determine the elemental abundances for all our stars. We use the 1D LTE stellar atmosphere models from (Castelli & Kurucz 2003) along with the radiative transfer code MOOG that includes scattering (Snedden 1973; Sobeck et al. 2011) and the Barklem et al. (2000) damping constants. The spectra were analyzed using SMHR³ (Casey 2014; Ji et al. 2020), which provides an interface for fitting equivalent widths, interpolating the model atmospheres, and running MOOG to determine abundances from equivalent widths and spectrum synthesis. Equivalent widths are measured semi-automatically using a model that fits each absorption line with a Gaussian profile multiplied by a linear continuum model. The measurements are then manually inspected to verify each line or apply corrections. Abundances of synthesized lines are matched through a χ^2 minimization by optimizing the abundance of a given element, the local continuum, a Gaussian smoothing kernel, and accounting for any small v_{helio} offsets. Each fit is again visually examined, and poor-fitting spectral regions are masked and refit. Further details are given in Ji et al. (2020).

We adopted the linelist from the works of the *R*-Process Alliance with updated $\log gf$ values (Roederer et al. 2018), generated with linemake code (Placco et al. 2021). We include hyperfine splitting from linemake as well. We assume isotopic ratios of $^{12}\text{C}/^{13}\text{C} = 4$ given that the majority of the sample is near the tip of the red giant branch and have experienced deep mixing processes (e.g., Skowronski et al. 2023). For Ba and Eu, we assume pure *r*-process isotopes from Sneden et al. (2008) given the low metallicity of our sample.

We measured up to 20 elements, including C, Na I, Mg I, Al I, Si I, Ca I, Sc II, Ti II, Cr I, Mn I, Co I, Ni I,

³ <https://github.com/andycasey/smhr>

Table 2. Stellar parameters of the 37 Sgr stars in this study.

Star Name	T_{eff}	$\sigma_{T_{\text{eff}}}$	$\log g$	$\sigma_{\log g}$	v_t	σ_{v_t}	[Fe/H]	$\sigma_{[\text{Fe}/\text{H}]}$
	(K)	(K)	(cgs)	(cgs)	(km s^{-1})	(km s^{-1})	(dex)	(dex)
Stream								
○ Sgr421	4655	122	1.14	0.20	2.2	0.3	-2.81	0.16
○ Sgr422	5026	123	2.06	0.20	1.9	0.3	-1.93	0.19
○ Sgr423	4722	122	1.29	0.20	2.1	0.3	-2.52	0.09
○ Sgr424	4814	122	1.50	0.20	1.9	0.3	-2.43	0.17
○ Sgr426	4750	122	1.36	0.20	2.2	0.3	-2.93	0.14
○ Sgr428	4790	123	1.48	0.20	2.2	0.3	-2.39	0.18
○ Sgr430	4280	122	0.40	0.20	2.2	0.3	-2.42	0.21
○ Sgr431	4659	123	1.15	0.20	2.1	0.4	-2.82	0.18
○ Sgr434	4846	123	1.57	0.20	1.9	0.3	-2.70	0.16
○ Sgr438	5274	123	2.60	0.20	1.4	0.3	-2.53	0.16
○ Sgr441	4334	122	0.47	0.20	2.5	0.3	-2.78	0.21
○ Sgr442	4697	122	1.24	0.20	2.0	0.3	-3.21	0.16
○ Sgr449	4759	122	1.33	0.20	1.9	0.3	-3.29	0.15
○ Sgr452	4516	123	0.84	0.20	2.4	0.3	-3.16	0.17
○ Sgr453	4313	122	0.59	0.21	2.1	0.3	-2.25	0.23
Core								
● Sgr459	4363	122	0.53	0.20	2.3	0.3	-2.66	0.21
● Sgr460	4717	123	1.28	0.20	2.2	0.3	-3.00	0.16
● Sgr462	4625	122	1.07	0.20	2.2	0.3	-2.83	0.16
● Sgr463	4423	122	0.65	0.20	2.2	0.3	-2.69	0.19
● Sgr468	4491	122	0.79	0.20	2.2	0.3	-2.57	0.20
● Sgr2	4609	122	1.04	0.20	2.2	0.3	-2.66	0.17
● Sgr471	4542	122	0.89	0.20	2.4	0.3	-3.14	0.17
● Sgr476	4371	122	0.54	0.20	1.9	0.3	-2.88	0.22
● Sgr69	4401	122	0.60	0.20	2.5	0.3	-2.68	0.22
● Sgr482	4604	122	1.02	0.20	2.1	0.3	-2.74	0.17
● Sgr4	4379	122	0.56	0.20	2.5	0.4	-3.10	0.19
● Sgr38	4784	123	1.43	0.20	2.0	0.3	-2.72	0.17
● Sgr484	4697	123	1.23	0.20	2.0	0.3	-2.94	0.15
● Sgr488	4492	122	0.79	0.20	2.3	0.3	-3.02	0.20
● Sgr492	4466	122	0.73	0.20	2.5	0.6	-2.81	0.25
● Sgr495	4412	122	0.63	0.20	2.3	0.3	-2.96	0.17
● Sgr496	4613	122	1.04	0.20	1.9	0.3	-2.95	0.18
● Sgr9	4589	122	1.30	0.20	2.1	0.3	-1.85	0.20
● Sgr504	4517	122	0.84	0.20	2.2	0.3	-2.67	0.19
● Sgr505	4524	122	0.85	0.20	2.2	0.3	-3.06	0.17
● Sgr509	4699	122	1.24	0.20	2.0	0.3	-3.18	0.16
● Sgr512	4614	122	1.05	0.20	2.0	0.3	-3.03	0.16

Zn I, Sr II, Y II, Zr II, Ba II, La II, Eu II, and Dy II. We provide our final derived abundances in Table 3. The abundances of the α -elements, as well as Na and Al, are shown in Figure 2. The Fe-peak elements are presented in Figure 3, while the neutron capture elements are shown in Figure 4. We note that we do not include the non-LTE correction for the following species known to be affected by departures from LTE: Na I, Al I, Cr I, and Mn I. This allows for a more consistent comparison of our results with those in the literature, which are largely presented without a non-LTE correction.

We estimate the uncertainties associated with our abundance measurements following the treatment detailed in Ji et al. (2020), with the exception of the cor-

relation matrix between stellar parameters (Equation 4 of Ji et al. 2020). The correlation matrix depends on the specific stellar sample and thus should be redetermined for our Sgr sample. We find no significant differences in the final estimated total uncertainties for most elements when not incorporating the correlation (i.e., making the matrix diagonal). Thus, we simply report statistical uncertainty for each element estimated from the weighted standard error in the individual line measurements for a given element. Systematic uncertainties are estimated by varying the model atmosphere stellar parameters based on the total uncertainties reported in Table 2. An example star (Sgr421) is shown in Table 4 to demonstrate the typical values for the systematic uncer-

Table 3. Chemical Abundances for the Sgr sample with the number of lines used for each element and associated total uncertainties.

El.	N	log $\epsilon(X)$	σ	[X/H]	$\sigma_{[X/H]}$	[X/Fe]	$\sigma_{[X/Fe]}$
Sgr2							
Na I	2	3.96	0.07	-2.28	0.25	0.38	0.12
Mg I	4	5.25	0.13	-2.35	0.16	0.31	0.08
Al I	2	3.37	0.22	-3.09	0.42	-0.43	0.29
Si I	2	5.34	0.21	-2.17	0.26	0.49	0.16
Ca I	15	3.97	0.16	-2.37	0.13	0.29	0.06
Sc II	7	0.52	0.12	-2.63	0.10	-0.08	0.06
Ti I	14	2.30	0.17	-2.65	0.20	0.01	0.07
Ti II	29	2.57	0.15	-2.38	0.12	0.17	0.07
V I	2	0.95	0.01	-2.99	0.12	-0.33	0.10
V II	2	1.16	0.10	-2.77	0.10	-0.22	0.11
Cr I	9	2.80	0.12	-2.84	0.19	-0.19	0.05
Cr II	3	3.07	0.14	-2.57	0.11	-0.02	0.10
Mn I	6	2.27	0.08	-3.16	0.11	-0.51	0.09
Fe I	154	4.84	0.20	-2.66	0.17	0.00	0.00
Fe II	15	4.95	0.12	-2.55	0.10	0.00	0.00
Co I	4	2.29	0.21	-2.70	0.17	-0.04	0.12
Ni I	4	3.59	0.21	-2.63	0.24	0.03	0.12
Zn I	1	2.06	0.00	-2.50	0.06	0.16	0.13
Sr II	2	0.61	0.11	-2.26	0.18	0.29	0.15
Y II	3	-0.59	0.07	-2.80	0.10	-0.25	0.09
Zr II	1	0.14	0.00	-2.44	0.10	0.11	0.06
Ba II	5	-0.94	0.17	-3.12	0.13	-0.57	0.10
La II	3	-1.94	0.10	-3.04	0.10	-0.49	0.13
C-H	2	5.44	0.01	-2.99	0.29	-0.34	0.19
C-N	1	6.22	0.00	-1.61	0.40	1.05	0.27
Eu II	3	-2.27	...	-2.79	...	-0.23	...
Dy II	1	-0.60	...	-1.70	...	0.86	...

NOTE—The complete version of Table 3 is available in the online edition of the journal. A short version with an example star is included here to demonstrate its form and content.

tainties of each element from different stellar parameter uncertainties.

4. DISCUSSION AND INTERPRETATION

In this section, we discuss the general features of the derived chemical abundances of the Sgr sample. We first compare our Sgr sample with the Milky Way halo, then move on to comparing with literature Sgr element abundances. We note for completeness that our sample in the Sgr stream could potentially contain halo star contaminants. However, without being able to further quantify the purity of our membership selection, we assume all stars as members for the purpose of our interpretation since low-metallicity interlopers from the Milky Way ought to be rare (Ivezić et al. 2008).

The overall distribution of light element abundances in our Sgr sample qualitatively matches that of the Milky Way halo at the same metallicity. This reflects extended chemical evolution in Sgr, not unlike what occurred in the early Milky Way. Among neutron-capture elements,

Table 4. Systematic elemental abundance uncertainties for an example star, Sgr421 (*Gaia* DR3 620763790933951488).

Element	ΔT_{eff}	$\Delta \log g$	Δv_t	$\Delta_{[\text{Fe}/\text{H}]}$	$\sigma_{\text{sys.}}$
	$\pm 122 \text{ K}$	$\pm 0.2 \text{ dex}$	$\pm 0.3 \text{ km s}^{-1}$	$\pm 0.16 \text{ dex}$	
Na I	0.15	-0.05	-0.16	-0.04	0.22
Mg I	0.11	-0.05	-0.05	-0.01	0.13
Al I	0.18	-0.06	-0.11	-0.03	0.22
Si I	0.17	-0.05	-0.05	-0.01	0.18
Ca I	0.10	-0.02	-0.04	-0.00	0.11
Sc II	-0.00	0.08	-0.06	0.01	0.10
Ti I	0.18	-0.02	-0.03	-0.01	0.18
Ti II	0.06	0.07	-0.08	0.02	0.12
V I	0.21	0.02	0.06	0.05	0.22
V II	-0.00	0.08	0.01	0.02	0.08
Cr I	0.16	-0.02	-0.02	-0.01	0.16
Cr II	-0.01	0.08	-0.01	0.01	0.08
Mn I	0.09	-0.04	-0.01	-0.01	0.10
Fe I	0.14	-0.02	-0.06	-0.01	0.16
Fe II	0.02	0.08	-0.03	0.02	0.09
Co I	0.14	-0.03	-0.03	-0.01	0.15
Ni I	0.15	-0.01	-0.01	-0.00	0.15
Zn I	0.04	0.03	-0.01	0.01	0.06
Sr II	0.06	0.04	-0.23	-0.02	0.24
Y II	0.08	0.08	-0.02	0.03	0.11
Zr II	0.04	0.09	0.01	0.02	0.10
Ba II	0.08	0.06	-0.13	-0.01	0.17
La II	0.07	0.07	-0.00	0.03	0.10
Eu II	0.08	0.07	0.01	0.03	0.11
Dy II	0.02	0.04	-0.07	-0.02	0.08
C-H	0.28	-0.07	0.02	0.06	0.29
C-N	0.33	-0.02	0.06	0.05	0.34

we also find general agreement with halo abundance trends. Half of our sample show the signature of the *r*-process process and corresponding enhancements in these elements. This signature suggests prior enrichment, likely by a neutron star merger or another astrophysical site of the *r*-process process. We discuss the implications of this further in Section 4.5 and 4.6.

In Figures 2-4, we then compare our measurements with those obtained by Sestito et al. (2024a), who also studied twelve very/extremely metal-poor stars in the Sgr core. Of the four overlapping stars between the Sestito et al. (2024a) and our core samples, three stars show qualitatively consistent measurements in most elements, except for Al I and Mn I. When comparing the trends seen in both two samples, systematic differences in the measurement techniques appear to drive the differences in these two abundances. Specifically, we adopted spectrum synthesis for measuring Al and Mn while Sestito et al. (2024a) used equivalent widths. We prefer the results from spectrum synthesis due to the proximity of the two Al lines, 3944 and 3961 Å, to strong hydrogen lines and hyperfine structure in Mn lines.

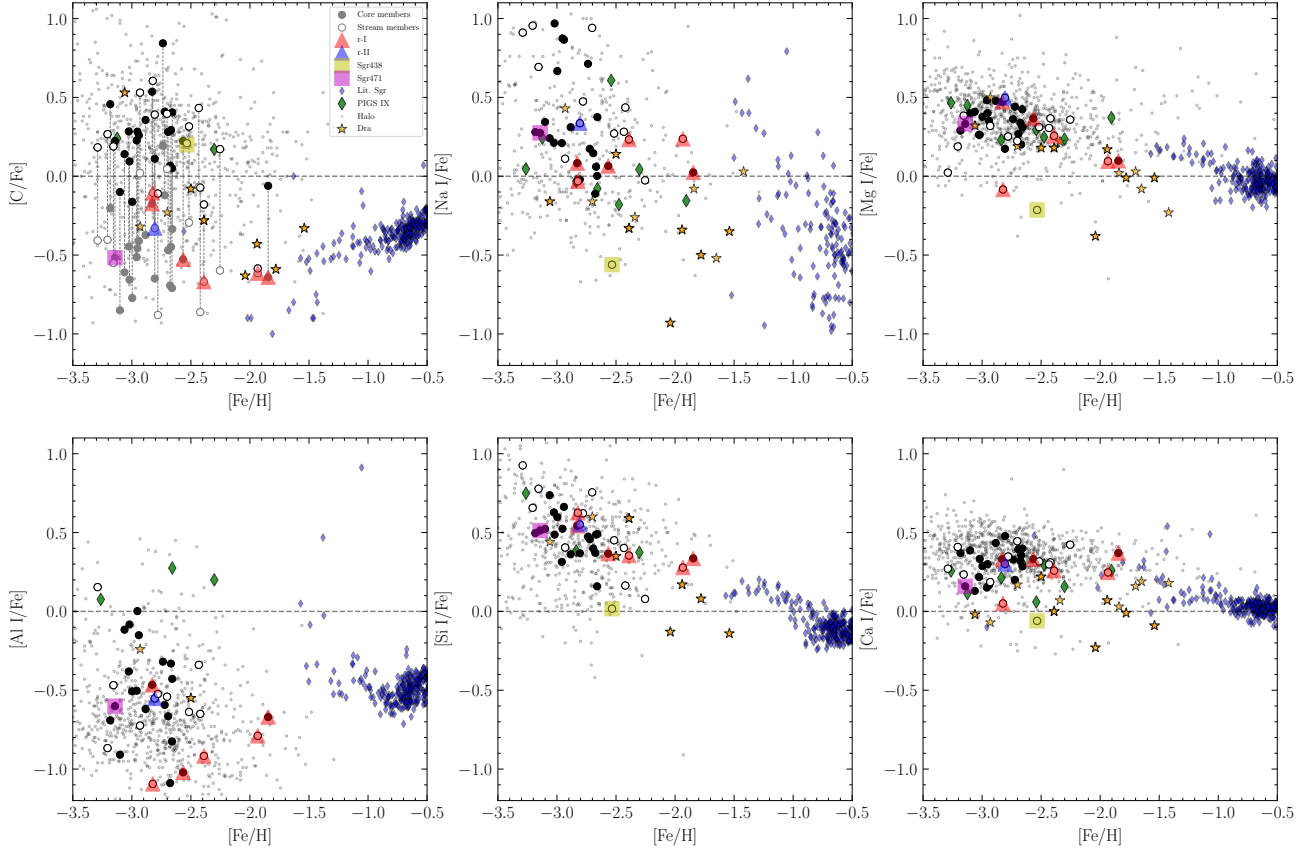


Figure 2. Light element abundances for the full Sgr sample. Stars in the Sgr streams are marked with open-face circles (\circ), whereas stars in the Sgr core are marked with black filled circles (\bullet). Literature values from Hansen et al. (2018) and APOGEE (Hasselquist et al. 2017) are shown as transparent blue diamonds. Sgr stars from Sestito et al. (2024a) are shown as green diamonds (PIGS IX). Halo stars compiled from JINABase (Abohalima & Frebel 2018) are shown as gray dots.

P185053–313317 in their study, which is Sgr471 in our sample, appears to display a drastically higher metallicity⁴. While we derived $[\text{Fe}/\text{H}] = -3.14$ for this star, Sestito et al. (2024a) reported $[\text{Fe}/\text{H}] = -1.22$. From examining three lines, Fe I 5171.6 Å, Ti II 5185 Å, Ti II 5188 Å in their Figure 2 and our MIKE spectrum, we find these three lines to have a significantly weaker line depths in our spectrum. As such our abundances are commensurate with our spectrum, and their results appear to reflect their spectrum, despite quoting the same coordinates for the object. Going forward, we thus continue to use our abundances for this star.

Furthermore, we investigate that five of the six stars with Eu measurements in the Sestito et al. (2024a) sample have detections and measurement at $[\text{Eu}/\text{Fe}] = 0.00$ dex. After excluding Sgr471, there are three stars left in common. For two stars, Sestito et al. (2024a) quote detections with measurements of $[\text{Eu}/\text{Fe}] = 0.00 \pm 0.20$ dex based on fitting with a fixed grid of 0.1 dex

intervals, whereas we find subsolar upper limits of ~ -0.25 dex. For internal consistency, we thus only plot Eu measurements derived in our analysis in Figure 4.

In the following Sections, we further discuss individual element abundances and their interpretation. We examine our Sgr sample in the $[\alpha/\text{Fe}]$ and $[\text{C}/\text{Fe}]$ vs. $[\text{Fe}/\text{H}]$ spaces as a probe of the contribution of early massive SNe in Sgr. Then we compare the abundances of the core and stream stars to assess potential differences. Finally, we report on the discovery of a population of r -process enhanced stars in both the core and the stream and discuss the signatures of early r -process enrichment in the Sgr progenitor.

4.1. α -element in Sgr and the star Sgr438

We begin by examining the α -elements in the Sgr sample. The α -element abundance ratios of most of our stars are enhanced at lower metallicity compared to those of the Sgr stars at higher metallicities ($[\text{Fe}/\text{H}] \gtrsim -1.5$) from APOGEE (Hasselquist et al. 2017; Hayes et al. 2020) and Hansen et al. (2018). The downturn from the higher to lower α -abundances appears to occur in between the $[\text{Fe}/\text{H}]$ ranges covered by the different samples but is likely due to the delayed enrichment in Fe

⁴ for unresolved reasons after checking the coordinate and potential contamination from the Moon or a second source, F. Sestito, priv. comm.

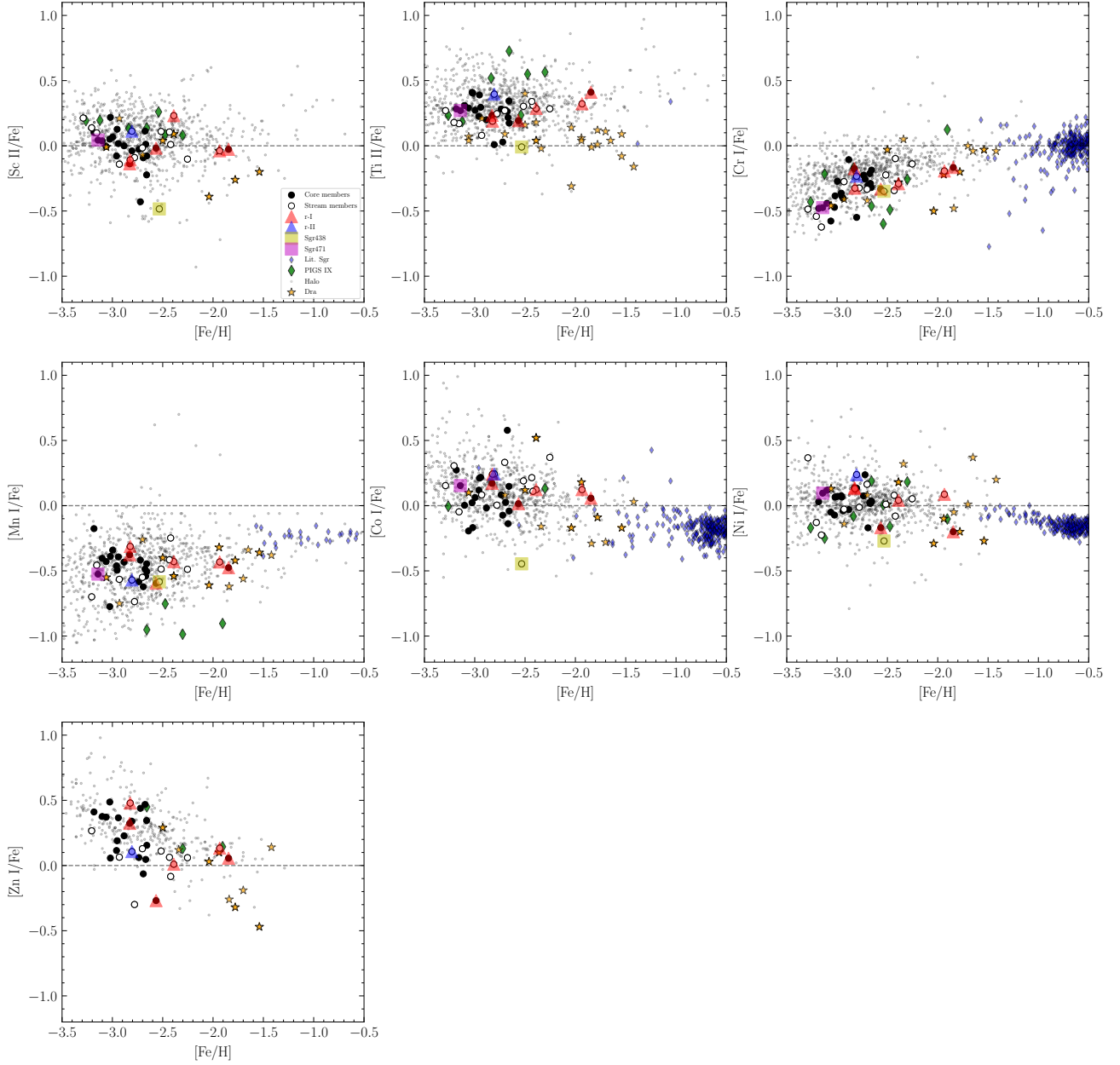


Figure 3. Fe-peak elements abundances for the full Sgr sample. Stars in the Sgr streams are marked with open-face circles (○), whereas stars in the Sgr core are marked with black filled circles (●). Literature values from Hansen et al. (2018) and APOGEE (Hasselquist et al. 2017) are shown as transparent blue diamonds. Sgr stars from Sestito et al. (2024a) are shown as green diamonds (PIGS IX). Halo stars compiled from JINAbase (Abohalima & Frebel 2018) are shown as gray dots.

peak element from SNe Ia. The metallicity/location of the downturn (i.e., α -knee) can be taken as an indicator of the stellar mass of the progenitor system. More massive systems are expected to experience more SN II contributing metals, evolving the system to a higher $[\text{Fe}/\text{H}]$ faster before the SN Ia onset. For our sample, we see no α -knee up to $[\text{Fe}/\text{H}] \sim -2.0$ which suggests that it must be at $[\text{Fe}/\text{H}] > -2.0$. This translates into a faster chemical enrichment history for Sgr compared to smaller dwarf galaxies. This is principally consistent with the estimate of the Sgr progenitor stellar mass of

$M_* \gtrsim 10^9 M_\odot$ (Majewski et al. 2003; Niederste-Ostholt et al. 2010; Vasiliev & Belokurov 2020). Other light element ratios also show a smooth trend from lower to higher metallicity, consistent with what would be expected for the chemical evolution of a high(er) stellar mass progenitor. Hence, the overall trends of our Sgr stars show a typical chemical evolution history for a galaxy of its mass, especially when combined with the abundance measurements at higher metallicities.

We then investigate stars that show α -element abundances distinct from the overall sample trends. We

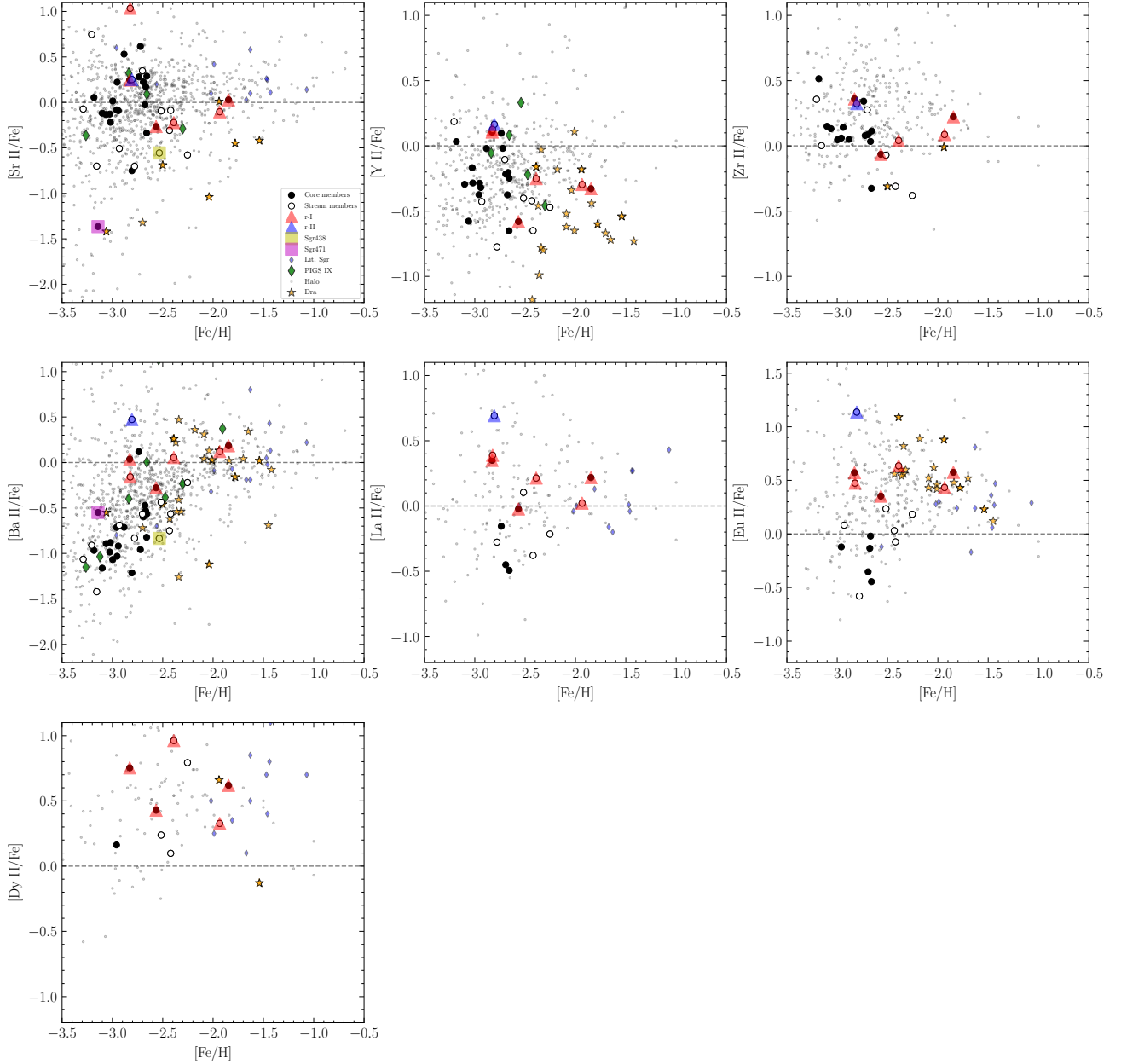


Figure 4. Neutron capture element abundances for the full Sgr sample. Stars in the Sgr streams are marked with open-face circles (\circ), whereas stars in the Sgr core are marked with black filled circles (\bullet). Literature values from Hansen et al. (2018) and APOGEE (Hasselquist et al. 2017) are shown as transparent blue diamonds. Sgr stars from Sestito et al. (2024a) are shown as green diamonds (PIGS IX). Halo stars compiled from JINAbase (Abohalima & Frebel 2018) are shown as gray dots.

compute and compare the averaged α -element measurements (Mg, Si, Ca, and Ti) to account for potential abundance variations before assessing the origins of these stars.

Several core and stream stars have low abundances only in a single α -element, with their average α -abundance broadly agreeing with the overall trend. Hence, we do not further discuss them. But one star, Sgr438, has consistently low α abundances in all four elements (~ -0.1), which is easily apparent in Figure 2 and the $[\alpha/\text{Fe}]$ vs. $[\text{Fe}/\text{H}]$ panel in Figure 5. Sgr438 has

$[\text{Fe}/\text{H}] = -2.53$ and $[\text{Mg}/\text{Fe}] = -0.21$, $[\text{Si}/\text{Fe}] = 0.02$, $[\text{Ca}/\text{Fe}] = -0.06$, and $[\text{Ti}/\text{Fe}] = -0.01$ for a low combined $[\alpha/\text{Fe}] = -0.06 \pm 0.07$, compared with the rest of the sample at $[\alpha/\text{Fe}] \sim 0.30$. Low α abundances are generally thought of as the results of enrichment by Type Ia SNe which contribute iron-peak elements to the gas. Type Ia SNe contributions at relatively low metallicity suggest that our star formed in a dwarf galaxy progenitor that underwent slower chemical enrichment than what the Sgr experienced. We thus speculate that this dwarf progenitor was less massive than the Sgr progen-

itor and one of its building blocks. Likewise, the star’s low Na, Sc, Co, and Sr abundances at $[X/Fe] \sim -0.5$ show qualitative consistent behavior with measurements from the classical dwarf galaxy Draco (Cohen & Huang 2009), as shown in Figures 2-4. Sgr438 is thus likely formed in a lower-mass dwarf progenitor with a stellar mass similar to that of Draco ($M_* \sim 10^{5.5} M_\odot$; Odenkirchen et al. 2001) rather than in-situ. In addition, its host dwarf galaxy must have merged into Sgr before its infall into the Milky Way, given that it now belongs to the Sgr stream.

4.2. Absence of CEMP stars

We measured the $[C/Fe]$ abundance using the CH bandhead at 4313 Å and the feature at 4323 Å. On average, our Sgr sample of cool red giants displays $[C/Fe] \sim -0.5$ dex. We follow Placco et al. (2014) to correct the effect of evolutionary status on observed C abundances. The correction ranges between 0.4 and 0.7 depending on the position of the stars along the red giant branch, i.e., $\log g$. The corrected $[C/Fe]$ values are shown in the first panel of Figure 2. The bulk of the sample has corrected $[C/Fe] \sim 0.2$, with a spread of 0.3 dex. Interestingly, we find only one star (Sgr482) with an enhanced level of C ($[C/Fe] = 0.84$) in both the core and the stream after the correction, as shown in the first panel of Figure 2. This star can now be classified as a carbon-enhanced metal-poor (CEMP) star with $[C/Fe] > 0.7$ (Aoki et al. 2007). The resulting fraction of CEMP star in Sgr is 1 in 37 for our sample, which is exceedingly small. This is in stark contrast to what is found among metal-poor halo stars, which generally show a large fraction of 20-40% of CEMP stars with $[Fe/H] \lesssim -3$ (Placco et al. 2014).

We compare our $[C/Fe]$ with those reported Sestito et al. (2024a) and Sestito et al. (2024b) and find overall good agreement for the $[C/Fe]$ across the Sgr samples. Sestito et al. (2024b) utilized medium-resolution spectroscopy for ~ 350 metal-poor stars $[Fe/H] \lesssim -2.5$ in the Sgr core to study the fraction of CEMP stars in the Sgr. Their corrected average $[C/Fe]$ abundances for stars is $\langle [C/Fe] \rangle \sim 0.0 \pm 0.1$ dex. Only three or four CEMP stars were identified in the Sestito et al. (2024b) sample, and all are classified as potentially *s*-process enriched CEMP stars (CEMP-s), suggesting an absence of CEMP stars in the Sgr core relative to the Milky Way stellar halo population. Similarly, comparing our C abundances with those obtained from high-resolution spectra by Sestito et al. (2024a), as shown in Figure 2, we find a consistent behavior across the two samples with a low to absent CEMP fraction.

We note that the photometric metallicity selection using the Ca II K feature, as is done in this study, can principally be biased against finding CEMP stars due to the presence of the CN molecular absorption feature near the Ca II K line and depending on the stellar parameters (Starkenburger et al. 2017b; Chiti et al. 2020a). A larger carbon abundance and lower effective temperature lead

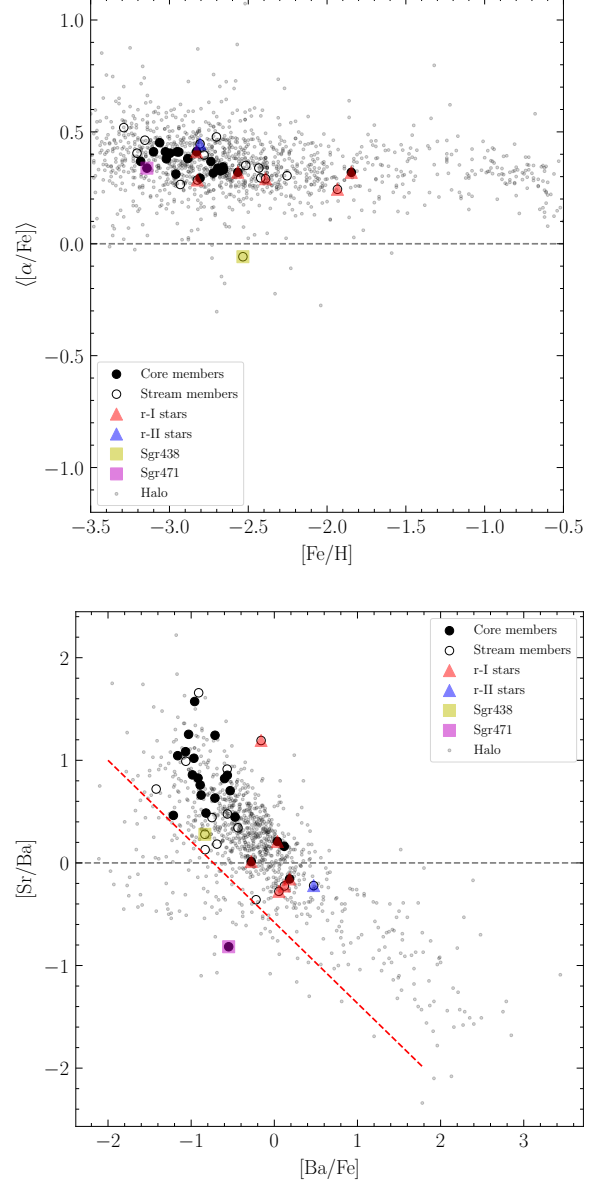


Figure 5. Average $[\alpha/Fe]$ vs. $[Fe/H]$ (top) and $[Sr/Ba]$ vs. $[Ba/Fe]$ (bottom) abundances for our Sgr stars. Legends are the same as Figure 2. The top panel showcases the one star, Sgr438 with low $[\alpha/Fe]$ abundances, whose origin we discuss in detail in Section 4.1. The bottom panel shows one potential UFD star, Sgr471, with the rest of the sample distributed above the empirical cut.

to stronger CN absorption in the spectrum. This can cause an artificially higher photometric metallicity measurement, making stars with strong CN features appear more metal-rich than they actually are. Studies have shown that the most extreme CEMP stars would likely be excluded when using this technique (Ardern-Arentsen et al. 2024; Chiti et al. 2024), but these selection effects likely do not completely eliminate CEMP stars (with

corrected C abundances) with moderate enhancements in the T_{eff} and $\log g$ range of our sample, as argued in Chiti et al. (2024) and Sestito et al. (2024b).

The differences in CEMP fraction between the Sgr and the Milky Way halo stars suggest different early chemical enrichment in the Sgr progenitor compared to the Milky Way and its progenitors. Chemical enrichment models and SNe nucleosynthesis calculations produce enhanced [C/Fe] ratios ([C/Fe] > 2.0) for faint CCSNe that undergo a fall-back explosion, during which some of the Fe falls back on the nascent remnant (Tsujiyama & Shige-yama 2003; Umeda & Nomoto 2003; Cooke & Madau 2014). This results in a lower Fe yield, thus increasing the [C/Fe] ratio. The absence of CEMP stars in the Sgr may suggest a significant lack of faint SNe progenitors dominating the enrichment of its early gas. Instead, regular core-collapse SNe may rather have produced the observed carbon. To test this idea, we use *StarFit*⁵ to fit SN nucleosynthesis yield predictions from Heger & Woosley (2010) to the average abundance patterns of both the core and stream samples. Overall, the data was matched well, in both cases, by the yields of a relatively luminous SN with a progenitor mass of $15.8 M_{\odot}$ and high explosion energy of 1.8×10^{51} erg. At least qualitatively, this supports that there was no significant contribution from faint CCSNe. A similar behavior of carbon abundances has also been observed in low metallicity stars in other dwarf galaxies in the Milky Way, such as the LMC (Chiti et al. 2024), Draco (Cohen & Huang 2009), and Sculptor (Skúladóttir et al. 2024).

4.3. Comparison of core and stream stars

Λ CDM predicts that galaxies form through hierarchical assembly, with accreted stars typically residing further away from the center of the host galaxy (Bullock & Johnston 2005; Cooper et al. 2010, 2013). At the same time, tidal disruption strips away stellar populations at the outskirts of the disrupted galaxy first. Thus, in the case of the Sgr, we would expect a higher fraction of stars in the Sgr stream to be accreted rather than formed in-situ compared to the stars still present in the Sgr core (Helmi 2020). We, therefore, compare the element abundance trends between the core and stream stars to examine potential differences due to past accretion events to Sgr.

For most elements examined in this study, there are no significant abundance differences between the core and stream samples, as shown in Figure 6. To quantify this further, we obtained mean abundances for each sample (Table 5); there is no significant difference within 1σ for all elements. These similarities suggest that the earliest progenitors that contributed to the chemical enrichment of both the early Sgr and any smaller galaxies that accreted to Sgr at early times were largely the same

Table 5. The mean abundances and corresponding spreads for the Sgr stars in core vs. stream.

Element	Mean		Spread		Number	
	Stream	Core	Stream	Core	Stream	Core
[C/Fe]	0.18	0.24	0.30	0.22	15	22
[Na I/Fe]	0.35	0.31	0.40	0.31	15	22
[Mg I/Fe]	0.22	0.34	0.18	0.10	15	22
[Al I/Fe]	-0.59	-0.44	0.33	0.29	14	21
[Si I/Fe]	0.45	0.46	0.26	0.13	15	22
[Ca I/Fe]	0.27	0.31	0.13	0.09	15	22
[Sc II/Fe]	0.01	-0.01	0.17	0.13	15	22
[Ti II/Fe]	0.24	0.26	0.10	0.10	15	22
[Cr I/Fe]	-0.32	-0.33	0.14	0.13	15	22
[Mn I/Fe]	-0.50	-0.47	0.13	0.12	14	21
[Co I/Fe]	0.12	0.06	0.18	0.15	15	21
[Ni I/Fe]	0.03	0.02	0.16	0.11	15	22
[Zn I/Fe]	0.08	0.22	0.18	0.20	12	20
[Sr II/Fe]	-0.11	-0.05	0.49	0.42	15	22
[Y II/Fe]	-0.29	-0.27	0.30	0.22	12	19
[Zr II/Fe]	0.05	0.14	0.24	0.18	9	16
[Ba II/Fe]	-0.52	-0.68	0.48	0.39	15	22
[La II/Fe]	0.06	-0.12	0.34	0.32	8	6
[Eu II/Fe]	-0.04	-0.24	0.43	0.37	10	8
[Dy II/Fe]	0.61	0.48	0.43	0.21	6	4

kind. Alternatively, similar chemical abundances could arise from a lack of major accretion events to Sgr (i.e., it evolved in isolation). The stars we observe would thus be all formed in situ, resulting in the same kind of chemical enrichment history across the core and stream populations. Either way, as a result, our metal-poor samples reflect early enrichment by SN II.

4.4. An UFD-like star in the core: Sgr471

As noted, we can search for signatures of accretion from smaller dwarf galaxies onto Sgr to probe the low-mass end of the galaxy mass function. Stellar abundances of surviving UFD stars have been shown to display unique signatures (Frebel 2018; Simon 2019; Ji et al. 2019) especially among neutron-capture elements. Due to their low masses, which preclude forming enough stars to sample rare enrichment events (e.g., early r -process), nearly all UFDs have extremely low levels of Sr and Ba (e.g., Ji et al. 2019). They also have a characteristic lower [Sr/Ba] ratio compared with stars formed in more massive systems. We thus examine our Sgr sample for signs of these signatures that reflect formation in UFD-mass environments.

We find that one star, Sgr471, displays this characteristic signature in its neutron-capture elements and thus label it as likely originating from a UFD. Specifically, Sgr471 shows a clear departure from the bulk of the Milky Way halo sample and the Sgr sample in the [Sr/Ba] vs. [Ba/Fe] space, as can be seen in the

⁵ <https://starfit.org/>

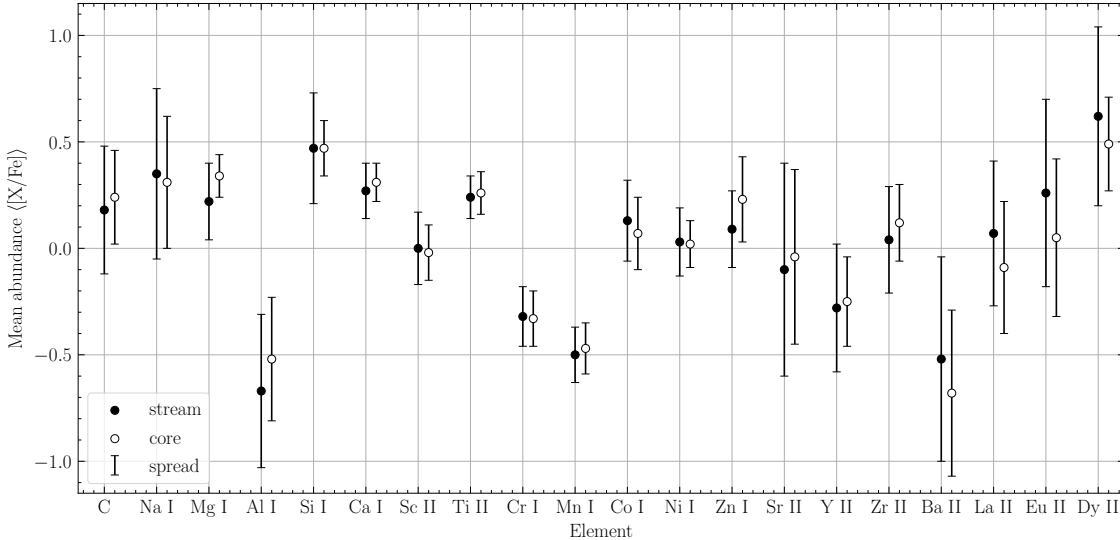


Figure 6. Comparison of means and spreads of various element abundances of all the stars located in the Sgr core and the stream.

bottom panel of Figure 5. Sgr471 has $[Fe/H] = -2.53$, $[Sr/H] = -4.51$, and $[Ba/H] = -3.69$ for a low $[Sr/Ba] = -0.82 \pm 0.26$. The low $[Sr/Ba]$ value suggests this star likely formed in a UFD environment before being accreted to Sgr. For completeness, we note that this star is unlikely to be a Milky Way halo foreground contaminant as it is located in the Sgr core.

Given the overall sample size of 37 stars and assuming no contaminants, we estimate a contribution of $1/37 (\sim 3\%)$ of the stellar mass of Sgr’s low metallicity population (restricted to $[Fe/H] \lesssim -2$) was accreted from UFDs. This estimate should be regarded as uncertain due to our small sample size and rarity of the putative accretion event. Using the Clopper–Pearson interval (Clopper & Pearson 1934), we find the 95% confidence interval ranges from 0.1% to 14% for the accreted metal-poor mass fraction of material with $[Fe/H] \lesssim -2$. Nonetheless, even at 14%, we expect the contribution to the total stellar mass of Sgr from UFDs to be minimal as the majority of the Sgr stars have $[Fe/H] \gtrsim -2$. Assuming $\sim 3\%$ of the Sgr stars have $[Fe/H] \lesssim -2$, estimated from photometric metallicity distribution function from Vitali et al. (2022), the UFD contribution to the total stellar mass of the Sgr can be qualitatively constrained to $\lesssim 0.5\%$.

4.5. *r*-process enhanced stars and their origin

We now examine the overall abundance of heavy elements in stars in our sample. In all stars, we measure Sr, Ba; for a subset of stars, we also determine Y, Zr, La, Eu, and Dy. For these latter stars, we compare their abundance pattern with that of the scaled solar *r*-process pattern. This comparison reveals that Sgr does indeed contain a population of *r*-process-enhanced stars. Following the recommendation from Holmbeck et al. (2020), we

Table 6. Ba and Eu abundances of the eight *r*-process-enhanced stars discussed in Section 4.5.

Star Name	[Fe/H] (dex)	[Ba/Fe] (dex)	[Eu/Fe] (dex)	[Ba/Eu] (dex)	Classification
● Sgr9	-1.85	0.18	0.58	-0.39	r-I
○ Sgr421	-2.81	0.47	1.14	-0.66	r-II
○ Sgr422	-1.93	0.12	0.43	-0.31	r-I
○ Sgr423	-2.52	-0.44	0.24	-0.67	\sim r-I
○ Sgr428	-2.39	0.06	0.64	-0.58	r-I, \sim r-II
○ Sgr431	-2.82	-0.16	0.47	-0.63	r-I
● Sgr462	-2.83	0.04	0.57	-0.53	r-I
● Sgr468	-2.57	-0.28	0.35	-0.63	r-I

group *r*-process-enhanced stars into two categories: r-II stars as having $[Eu/Fe] \gtrsim 0.7$, and r-I stars as having $0.7 \gtrsim [Eu/Fe] \gtrsim 0.3$.

We find one r-II star (Sgr421) and six r-I stars (Sgr9, Sgr422, Sgr428, Sgr431, Sgr462, and Sgr468) in our sample. We additionally consider Sgr423 as a r-I star for the remaining discussion due to its $[Ba/Eu] = -0.67$ that reflects the *r*-process ratio, and a $[Eu/Fe] = 0.24 \pm 0.08$ is consistent with being an r-I star within $1-\sigma$. Five of these stars are in the Sgr stream, and three are in the Sgr core. The relevant element abundances are shown in Table 6.

These stars thus probe the origins of heavy element nucleosynthesis associated with the *r*-process in the early Sgr. To investigate the *r*-process in more detail, we compare the measured heavy element abundances of

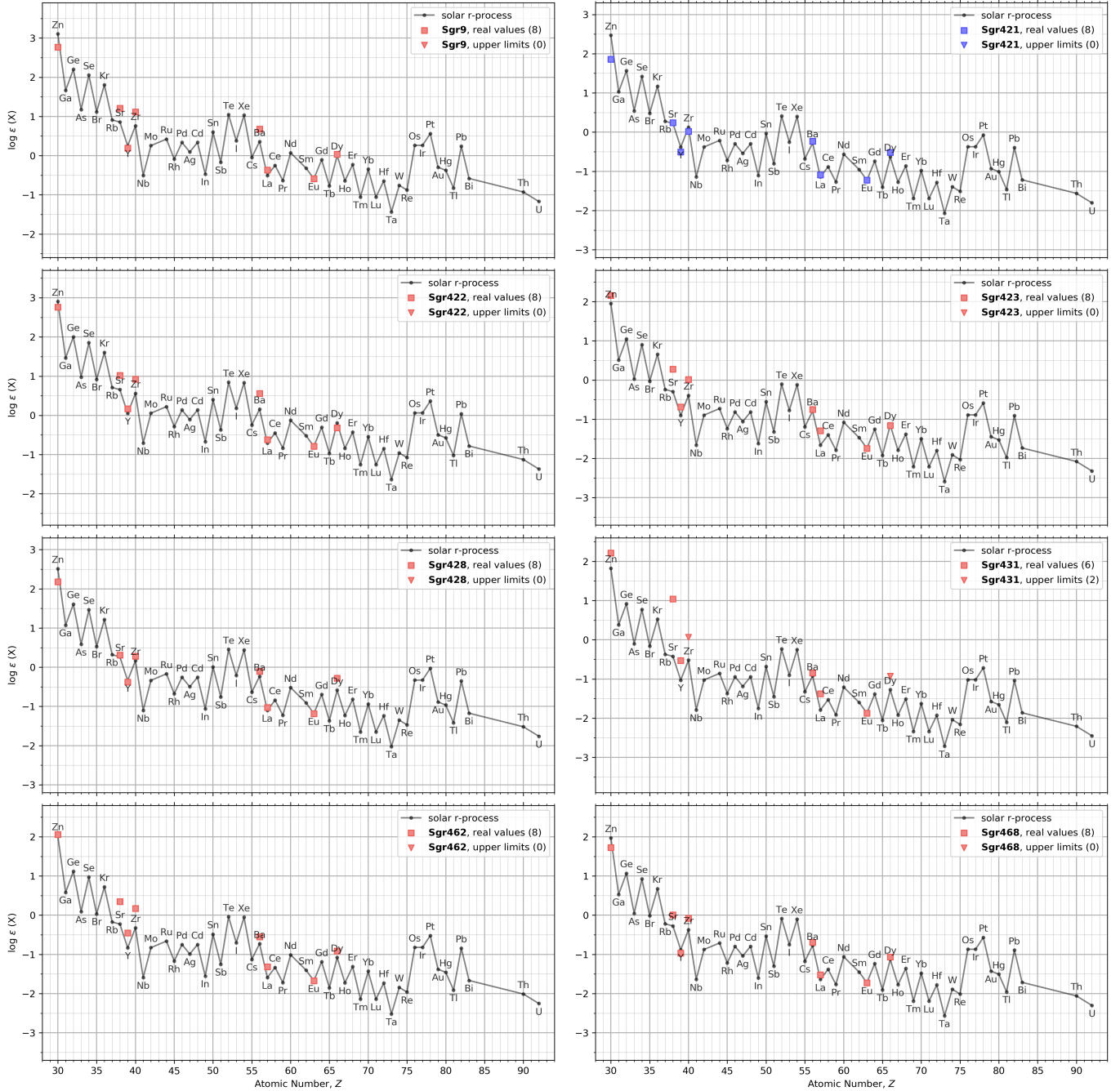


Figure 7. Heavy element abundance patterns of six r-I stars (Sgr9, Sgr428, Sgr462, Sgr431, Sgr422, Sgr468) and one r-II star (Sgr421), compared to the scaled (normalized to the stellar europium, Eu, abundance) solar r -process abundance pattern (black line).

these eight stars with the scaled solar r -process pattern (Sneden et al. 2008), as shown in Figure 7.

Our confirmed r -process stars cover a range of $-0.7 < [\text{Ba}/\text{Eu}] < -0.3$. Further, there is overall good agreement between the scaled solar r -process pattern and observed abundances for elements with atomic numbers higher than Ba. The pure r -process yields a $[\text{Ba}/\text{Eu}]$ ratio of -0.7 with higher values indicating the exist-

tence of s -process, as s -process primarily injects Ba into the environment (Sneden et al. 2008). Yet, assuming solar r -process and s -process patterns (Sneden et al. 2008), the Eu contribution from r -process is estimated to be ~ 150 times that from s -process, in terms of Eu mass. This estimate is an over-simplification because the s -process pattern is somewhat metallicity dependent (e.g., Lugaro et al. 2012), but it nevertheless illustrates

that the Eu in these eight stars is predominantly produced in *r*-process events, confirming the operation of *r*-process progenitor events. We also examined the remaining non-rI and rII stars with available Ba and Eu values for their [Ba/Eu] to check whether their abundance patterns may reveal a *r*-process contribution. We find over half of the remaining stars have [Ba/Eu] consistent with the scaled solar *r*-process pattern.

Additionally, six r-I stars (except for Sgr428) show Sr and Zr abundances higher than the scaled *r*-process abundance. This has also been observed in other *r*-process stars (Roederer et al. 2010). This excess suggests an additional contribution of CCSNe to these light neutron-capture elements, likely through a limited *r*-process that preferentially produces Sr, Y and Zr (Travaglio et al. 2004; Honda et al. 2006; Wanajo et al. 2011). In addition, we find one star, Sgr431, with a Sr excess of 1.5 dex above the scaled solar *r*-process pattern which also suggests some early Sr producing progenitor. Consequently, CCSNe nucleosynthesis undergoing a limited *r*-process must have occurred prior to the first regular *r*-process event.

The existence of eight confirmed *r*-process-enhanced stars across Sgr suggests that these stars either (1) formed in the Sgr progenitor after an early *r*-process enrichment or (2) formed in a former UFD with a clean environment before being accreted to the Sgr progenitor.

For the first interpretation, assuming the Sgr r-I and r-II stars are formed in-situ, the Sgr must have experienced early prompt *r*-process enrichment given their low metallicities ([Fe/H] $\lesssim -2$). The early prompt *r*-process enrichment could be neutron star mergers with short time delay and/or rare types of CCSNe (Siegel et al. 2019; Kobayashi et al. 2020; Yong et al. 2021; Cowan et al. 2021; Kobayashi et al. 2023). The roughly even split between core and stream among these stars indicates no preferred sites for these early enrichment events.

For the second interpretation, we discuss what fraction of these eight stars would be expected to be accreted from UFDs. Observations of the UFDs in the local group suggest that the occurrence rate of *r*-process events is low (~ 1 out of every 10-15 UFDs) (Ji et al. 2016). Such a low fraction of *r*-process enriched UFDs suggests that it is extremely unlikely that all eight stars discussed here are accretion from UFDs, i.e., $\gtrsim 20\%$ (> 8 out of 37) of the Sgr sample are accreted from UFDs. Specifically, we would expect to observe a factor of 10-15 more stars with low neutron-capture element abundances, given the low occurrence rate of *r*-process events in UFDs. Given our sample size of 37 stars and the UFD-like star Sgr471 (see Section 4.4) and given an estimated fraction of the accreted low metallicity population (restricted to [Fe/H] $\lesssim -2$) from UFDs of $\sim 3\%$, we estimate that plausibly one of the r-I or r-II stars could also be accreted from a UFD but not all of them.

Taking these two potential stars accreted from UFDs, qualitatively, the accreted stellar mass fraction from

UFDs to the total stellar mass remains minimal at $\lesssim 0.5\%$.

4.6. Early enrichment of the *r*-process in Sgr

In addition to individual stars, we examine the *r*-process enrichment process in the full Sgr sample, following a similar procedure described in Ou et al. (2024). Briefly speaking, the [Eu/Mg] vs. [Mg/H] space can be used to constrain the time evolution of *r*-process sources assuming that Eu is dominantly produced by *r*-process events, whereas Mg is dominantly produced by CCSNe events and traces the stellar formation of the galaxy. Thus, by assuming a galaxy has a relatively smooth star formation history, we can constrain the delay time distribution and *r*-process yield of potential *r*-process sources (neutron star mergers and/or rare type CCSNe) by examining the stars in the [Eu/Mg] vs. [Mg/H] space.

From Figure 8, we observe a large scatter in [Eu/Mg]. Six of the r-I and r-II stars discussed in Section 4.5 have [Eu/Mg] $\gtrsim 0.0$ dex. The elevation in Eu relative to Mg in these r-I and r-II stars indicates the existence of early *r*-process enrichment event(s) in the Sgr progenitor. On the other hand, a large fraction of the sample ($\sim 70\%$) has [Eu/Mg] $\lesssim 0.0$ dex (including upper limits), resulting in an average [Eu/Mg] $\lesssim 0.0$ dex for the full Sgr sample.

Recent observations of the LMC (Chiti et al. 2024; Oh et al. 2024) and the disrupted dwarf systems show evidence of a rise in [Eu/Mg] (Limberg et al. 2024; Ou et al. 2024), suggesting non-trivial *r*-process contribution from delayed sources. We thus examine our Sgr sample to search for a similar rise in Figure 8.

Because measurements for Eu abundances at high metallicity ([Mg/H] $\gtrsim -1.5$) are sparse and only available from Hansen et al. (2018), we combine our values with the measurements from GSE stars (Ou et al. 2024) for comparison. The GSE progenitor is estimated to have a similar stellar mass as the Sgr progenitor at $\sim 10^8$ - $10^9 M_\odot$, but the two systems had different star formation history, with the GSE forming stars for a much shorter period of time. As a consequence, assuming the *r*-process sources are similar in both systems, the rise should be present and span a similar range in [Eu/Mg] for Sgr and GSE. However, in Sgr, the rise is expected to start at lower [Mg/H] and span a larger range in [Mg/H] due to its longer star formation history (e.g., Vitali et al. 2024).

At first glance, we find no significant evidence for a rise in our Sgr sample alone, given the relatively narrow span in [Mg/H] and large scatter in [Eu/Mg]. When combined with the GSE sample, however, the extremely metal-poor Sgr sample appears to qualitatively continue the rising trend in the GSE towards lower [Eu/Mg] and [Mg/H]. Despite the presence of the early *r*-process enrichment events, the bulk measured [Eu/Mg] abundances for Sgr in this study are lower than the measurements for GSE stars, as well as the metal-rich sample

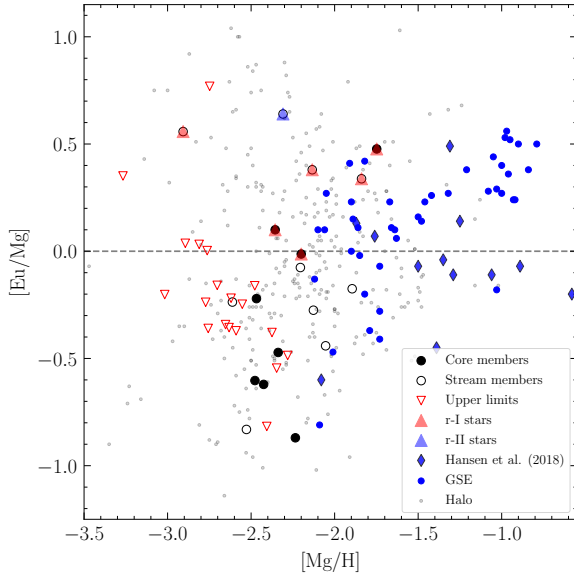


Figure 8. $[\text{Eu}/\text{Mg}]$ vs. $[\text{Mg}/\text{H}]$ for Sgr stars (black open/filled dots) in comparison with the GSE stars from [Ou et al. \(2024\)](#) (blue dots). Stars in the Sgr streams are marked. We also include measurements from [Hansen et al. \(2018\)](#) (red diamonds), with Ca as a proxy for Mg.

from [Hansen et al. \(2018\)](#). This behavior qualitatively supports that the delayed r -process sources must also be a dominant source for r -process enrichment. With more high metallicity data ($[\text{Mg}/\text{H}] > -2.0$), we can test for the existence of the rise within the Sgr stellar population.

5. SUMMARY

We investigate the chemical evolution of the Sgr dwarf galaxy by analyzing 37 stars, including 10 extremely metal-poor (EMP; $[\text{Fe}/\text{H}] \leq -3.0$), and 25 very metal-poor (VMP; $-3.0 \leq [\text{Fe}/\text{H}] \leq -2.0$) stars. These stars were drawn from both the Sgr core and its tidal streams, by utilizing photometric metallicity data from SkyMapper DR2 and the *Gaia* XP spectra, in addition to astrometric information from *Gaia* DR3. The chemical abundance patterns derived from these stars reveal several significant insights into Sgr’s formation and enrichment history.

- Analysis of their α -elements shows that most stars in the sample exhibit elevated $[\alpha/\text{Fe}]$ ratios at low metallicities, consistent with rapid enrichment by core-collapse supernovae (CCSNe). One star in the sample, Sgr438, exhibits significantly lower $[\alpha/\text{Fe}]$ ratios, suggesting it may have originated in a low-mass classical dwarf spheroidal progenitor that merged into Sgr.
- A comparison of elemental abundances between the Sgr core and stream populations shows no sta-

tistically significant differences. This uniformity suggests that the accreted galaxies had a similar chemical enrichment history as the Sgr progenitor, i.e., the Sgr experienced limited accretion of chemically distinct systems.

- The study also uncovers intriguing differences in Sgr’s chemical enrichment relative to the Milky Way halo. Corroborating other studies (e.g., [Sestito et al. 2024a,b](#)), we find fewer than expected CEMP stars, contrasting with the substantial fraction observed in the Milky Way halo population. This indicates differences in the early stellar populations or nucleosynthesis processes that enriched the early gas in Sgr, perhaps with a lower relative contribution of faint supernovae.
- One star, Sgr471, within the sample exhibits a distinct abundance pattern characteristic of stars that are found in UFDs, with notably low levels of neutron-capture element enrichment. We also find eight r-I and r-II stars, and argue that ~ 1 may plausibly be accreted from another UFD that was enriched by an r -process event. These discoveries highlight signatures of accretion of low-mass systems into Sgr during its assembly, consistent with hierarchical galaxy formation.
- Another key finding is the presence of widespread early neutron-capture element enrichment. Over half of the sample shows abundance patterns consistent with the scaled solar r -process pattern, with eight of them qualified as r-I or r-II stars. This high fraction of stars with the r -process pattern indicates that the Sgr progenitor experienced efficient r -process enrichment at an early stage of its evolution. Additionally, the $[\text{Eu}/\text{Mg}]$ versus $[\text{Mg}/\text{H}]$ abundances of the whole Sgr sample, when compared with the literature sample of more metal-rich stars from Sgr and GSE, reveals evidence for delayed r -process sources contributing to the chemical evolution of Sgr.

These findings underscore the importance of studying extremely metal-poor stars to better understand the chemical enrichment history and assembly history of dwarf galaxies. The results reveal that Sgr experienced an enrichment history characterized by early r -process events with plausible signatures of accretion from UFD-like and classical dwarf galaxy systems.

1 X. O. thanks the LSST Discovery Alliance Data Science
 2 Fellowship Program, which is funded by LSST Discovery
 3 Alliance, NSF Cybertraining Grant #1829740, the Brin-
 4 son Foundation, and the Moore Foundation; his partic-
 5 ipation in the program has benefited this work. X.O.,
 6 A.Y., and A.F. acknowledge support from NSF-AAG
 7 grant AST-2307436. A.C. is supported by a Brinson
 8 Prize Fellowship at UChicago/KICP.

9 The national facility capability for SkyMapper has
 10 been funded through ARC LIEF grant LE130100104
 11 from the Australian Research Council, awarded to the
 12 University of Sydney, the Australian National Univer-
 13 sity, Swinburne University of Technology, the Univer-
 14 sity of Queensland, the University of Western Australia,
 15 the University of Melbourne, Curtin University of Tech-
 16 nology, Monash University and the Australian Astro-
 17 nomical Observatory. SkyMapper is owned and oper-
 18 ated by The Australian National University’s Research
 19 School of Astronomy and Astrophysics. The survey data
 20 were processed and provided by the SkyMapper Team
 21 at ANU. The SkyMapper node of the All-Sky Virtual
 22 Observatory (ASVO) is hosted at the National Compu-
 23 tational Infrastructure (NCI). Development and support
 24 of the SkyMapper node of the ASVO has been funded
 25 in part by Astronomy Australia Limited (AAL) and the
 26 Australian Government through the Commonwealth’s
 27 Education Investment Fund (EIF) and National Col-
 28 laborative Research Infrastructure Strategy (NCRIS),
 29 particularly the National eResearch Collaboration Tools
 30 and Resources (NeCTAR) and the Australian National
 31 Data Service Projects (ANDS).

32 This work presents results from the European Space
 33 Agency (ESA) space mission *Gaia*. *Gaiadata* are be-
 34 ing processed by the *Gaia*Data Processing and Analy-
 35 sis Consortium (DPAC). Funding for the DPAC is pro-
 36 vided by national institutions, in particular the insti-
 37 tutions participating in the Gaia MultiLateral Agree-
 38 ment (MLA). The Gaia mission website is [https://](https://www.cosmos.esa.int/gaia)
 39 www.cosmos.esa.int/gaia. The Gaia archive website is
 40 <https://archives.esac.esa.int/gaia>.

41 This research has made use of NASA’s Astrophysics
 42 Data System Bibliographic Services; the arXiv pre-print
 43 server operated by Cornell University; the SIMBAD and
 44 VizieR databases hosted by the Strasbourg Astronomi-
 45 cal Data Center.

REFERENCES

- Abomalima, A., & Frebel, A. 2018, *ApJS*, 238, 36,
 doi: [10.3847/1538-4365/aadfe9](https://doi.org/10.3847/1538-4365/aadfe9)
- Aoki, W., Beers, T. C., Christlieb, N., et al. 2007, *ApJ*,
 655, 492, doi: [10.1086/509817](https://doi.org/10.1086/509817)
- Ardern-Arentsen, A., Kane, S. G., Belokurov, V., et al.
 2024, arXiv e-prints, arXiv:2410.11077,
 doi: [10.48550/arXiv.2410.11077](https://doi.org/10.48550/arXiv.2410.11077)
- Atzberger, K. R., Usman, S. A., Ji, A. P., et al. 2024, arXiv
 e-prints, arXiv:2410.17312,
 doi: [10.48550/arXiv.2410.17312](https://doi.org/10.48550/arXiv.2410.17312)

- Barklem, P. S., Piskunov, N., & O'Mara, B. J. 2000, *A&AS*, 142, 467, doi: [10.1051/aas:2000167](https://doi.org/10.1051/aas:2000167)
- Beers, T. C., & Christlieb, N. 2005, *ARA&A*, 43, 531, doi: [10.1146/annurev.astro.42.053102.134057](https://doi.org/10.1146/annurev.astro.42.053102.134057)
- Bellazzini, M., Ibata, R. A., Chapman, S. C., et al. 2008, *AJ*, 136, 1147, doi: [10.1088/0004-6256/136/3/1147](https://doi.org/10.1088/0004-6256/136/3/1147)
- Bernstein, R., Shtetman, S. A., Gunnels, S. M., Mochnacki, S., & Athey, A. E. 2003, in *Proc. SPIE*, Vol. 4841, *Instrument Design and Performance for Optical/Infrared Ground-based Telescopes*, ed. M. Iye & A. F. M. Moorwood, 1694–1704, doi: [10.1117/12.461502](https://doi.org/10.1117/12.461502)
- Bullock, J. S., & Johnston, K. V. 2005, *ApJ*, 635, 931, doi: [10.1086/497422](https://doi.org/10.1086/497422)
- Burbidge, E. M., Burbidge, G. R., Fowler, W. A., & Hoyle, F. 1957, *Reviews of Modern Physics*, 29, 547, doi: [10.1103/RevModPhys.29.547](https://doi.org/10.1103/RevModPhys.29.547)
- Carrasco, J. M., Weiler, M., Jordi, C., et al. 2021, *A&A*, 652, A86, doi: [10.1051/0004-6361/202141249](https://doi.org/10.1051/0004-6361/202141249)
- Casey, A. R. 2014, PhD thesis, Australian National University, Canberra
- Castelli, F., & Kurucz, R. L. 2003, in *Modelling of Stellar Atmospheres*, ed. N. Piskunov, W. W. Weiss, & D. F. Gray, Vol. 210, A20. <https://arxiv.org/abs/astro-ph/0405087>
- Ceccarelli, E., Mucciarelli, A., Massari, D., Bellazzini, M., & Matsuno, T. 2024, *A&A*, 691, A226, doi: [10.1051/0004-6361/202451377](https://doi.org/10.1051/0004-6361/202451377)
- Chiappini, C., Matteucci, F., & Gratton, R. 1997, *ApJ*, 477, 765, doi: [10.1086/303726](https://doi.org/10.1086/303726)
- Chiti, A., Frebel, A., Jerjen, H., Kim, D., & Norris, J. E. 2020a, *ApJ*, 891, 8, doi: [10.3847/1538-4357/ab6d72](https://doi.org/10.3847/1538-4357/ab6d72)
- Chiti, A., Frebel, A., Mardini, M. K., et al. 2021, *ApJS*, 254, 31, doi: [10.3847/1538-4365/abf73d](https://doi.org/10.3847/1538-4365/abf73d)
- Chiti, A., Hansen, K. Y., & Frebel, A. 2020b, *ApJ*, 901, 164, doi: [10.3847/1538-4357/abb1ae](https://doi.org/10.3847/1538-4357/abb1ae)
- . 2020c, *ApJ*, 901, 164, doi: [10.3847/1538-4357/abb1ae](https://doi.org/10.3847/1538-4357/abb1ae)
- Chiti, A., Mardini, M., Limberg, G., et al. 2024, *Nature Astronomy*, 8, 637, doi: [10.1038/s41550-024-02223-w](https://doi.org/10.1038/s41550-024-02223-w)
- Clopper, C. J., & Pearson, E. S. 1934, *Biometrika*, 26, 404. <http://www.jstor.org/stable/2331986>
- Cohen, J. G., & Huang, W. 2009, *ApJ*, 701, 1053, doi: [10.1088/0004-637X/701/2/1053](https://doi.org/10.1088/0004-637X/701/2/1053)
- Cooke, R. J., & Madau, P. 2014, *ApJ*, 791, 116, doi: [10.1088/0004-637X/791/2/116](https://doi.org/10.1088/0004-637X/791/2/116)
- Cooper, A. P., D'Souza, R., Kauffmann, G., et al. 2013, *MNRAS*, 434, 3348, doi: [10.1093/mnras/stt1245](https://doi.org/10.1093/mnras/stt1245)
- Cooper, A. P., Cole, S., Frenk, C. S., et al. 2010, *MNRAS*, 406, 744, doi: [10.1111/j.1365-2966.2010.16740.x](https://doi.org/10.1111/j.1365-2966.2010.16740.x)
- Cowan, J. J., Sneden, C., Lawler, J. E., et al. 2021, *Reviews of Modern Physics*, 93, 015002, doi: [10.1103/RevModPhys.93.015002](https://doi.org/10.1103/RevModPhys.93.015002)
- De Angeli, F., Weiler, M., Montegriffo, P., et al. 2023, *A&A*, 674, A2, doi: [10.1051/0004-6361/202243680](https://doi.org/10.1051/0004-6361/202243680)
- Deason, A. J., & Belokurov, V. 2024, *NewAR*, 99, 101706, doi: [10.1016/j.newar.2024.101706](https://doi.org/10.1016/j.newar.2024.101706)
- Dotter, A., Chaboyer, B., Jevremović, D., et al. 2008, *ApJS*, 178, 89, doi: [10.1086/589654](https://doi.org/10.1086/589654)
- Ernandes, H., Feuillet, D., Feltzing, S., & Skúladóttir, Á. 2024, *A&A*, 691, A333, doi: [10.1051/0004-6361/202450827](https://doi.org/10.1051/0004-6361/202450827)
- Ezzeddine, R., Frebel, A., & Plez, B. 2017, *ApJ*, 847, 142, doi: [10.3847/1538-4357/aa8875](https://doi.org/10.3847/1538-4357/aa8875)
- Ferguson, P. S., & Strigari, L. E. 2020, *MNRAS*, 495, 4124, doi: [10.1093/mnras/staa1404](https://doi.org/10.1093/mnras/staa1404)
- Frebel, A. 2018, *Annual Review of Nuclear and Particle Science*, 68, 237, doi: [10.1146/annurev-nucl-101917-021141](https://doi.org/10.1146/annurev-nucl-101917-021141)
- Frebel, A., Casey, A. R., Jacobson, H. R., & Yu, Q. 2013, *ApJ*, 769, 57, doi: [10.1088/0004-637X/769/1/57](https://doi.org/10.1088/0004-637X/769/1/57)
- Frebel, A., & Ji, A. P. 2023, arXiv e-prints, arXiv:2302.09188, doi: [10.48550/arXiv.2302.09188](https://doi.org/10.48550/arXiv.2302.09188)
- Frebel, A., & Norris, J. E. 2015, *ARA&A*, 53, 631, doi: [10.1146/annurev-astro-082214-122423](https://doi.org/10.1146/annurev-astro-082214-122423)
- Gaia Collaboration, Prusti, T., de Bruijne, J. H. J., et al. 2016, *A&A*, 595, A1, doi: [10.1051/0004-6361/201629272](https://doi.org/10.1051/0004-6361/201629272)
- Gaia Collaboration, Brown, A. G. A., Vallenari, A., et al. 2021, *A&A*, 649, A1, doi: [10.1051/0004-6361/202039657](https://doi.org/10.1051/0004-6361/202039657)
- Gaia Collaboration, Montegriffo, P., Bellazzini, M., et al. 2023, *A&A*, 674, A33, doi: [10.1051/0004-6361/202243709](https://doi.org/10.1051/0004-6361/202243709)
- Hansen, C. J., El-Souri, M., Monaco, L., et al. 2018, *ApJ*, 855, 83, doi: [10.3847/1538-4357/aa978f](https://doi.org/10.3847/1538-4357/aa978f)
- Hansen, T. T., Simon, J. D., Marshall, J. L., et al. 2017, *ApJ*, 838, 44, doi: [10.3847/1538-4357/aa634a](https://doi.org/10.3847/1538-4357/aa634a)
- Hansen, T. T., Marshall, J. L., Simon, J. D., et al. 2020, *ApJ*, 897, 183, doi: [10.3847/1538-4357/ab9643](https://doi.org/10.3847/1538-4357/ab9643)
- Hasselquist, S., Shetrone, M., Smith, V., et al. 2017, *ApJ*, 845, 162, doi: [10.3847/1538-4357/aa7ddc](https://doi.org/10.3847/1538-4357/aa7ddc)
- Hayes, C. R., Majewski, S. R., Hasselquist, S., et al. 2020, *ApJ*, 889, 63, doi: [10.3847/1538-4357/ab62ad](https://doi.org/10.3847/1538-4357/ab62ad)
- Heger, A., & Woosley, S. E. 2010, *ApJ*, 724, 341, doi: [10.1088/0004-637X/724/1/341](https://doi.org/10.1088/0004-637X/724/1/341)
- Helmi, A. 2020, *ARA&A*, 58, 205, doi: [10.1146/annurev-astro-032620-021917](https://doi.org/10.1146/annurev-astro-032620-021917)
- Hirai, Y., Beers, T. C., Lee, Y. S., et al. 2024, arXiv e-prints, arXiv:2410.11943, doi: [10.48550/arXiv.2410.11943](https://doi.org/10.48550/arXiv.2410.11943)
- Holmbeck, E. M., Hansen, T. T., Beers, T. C., et al. 2020, *ApJS*, 249, 30, doi: [10.3847/1538-4365/ab9c19](https://doi.org/10.3847/1538-4365/ab9c19)

- Honda, S., Aoki, W., Ishimaru, Y., Wanajo, S., & Ryan, S. G. 2006, *ApJ*, 643, 1180, doi: [10.1086/503195](https://doi.org/10.1086/503195)
- Ibata, R. A., Gilmore, G., & Irwin, M. J. 1994, *Nature*, 370, 194, doi: [10.1038/370194a0](https://doi.org/10.1038/370194a0)
- . 1995, *MNRAS*, 277, 781, doi: [10.1093/mnras/277.3.781](https://doi.org/10.1093/mnras/277.3.781)
- Ibata, R. A., Wyse, R. F. G., Gilmore, G., Irwin, M. J., & Suntzeff, N. B. 1997, *AJ*, 113, 634, doi: [10.1086/118283](https://doi.org/10.1086/118283)
- Ivezić, Ž., Sesar, B., Jurić, M., et al. 2008, *ApJ*, 684, 287, doi: [10.1086/589678](https://doi.org/10.1086/589678)
- Ji, A. P., Frebel, A., Chiti, A., & Simon, J. D. 2016, *Nature*, 531, 610, doi: [10.1038/nature17425](https://doi.org/10.1038/nature17425)
- Ji, A. P., Simon, J. D., Frebel, A., Venn, K. A., & Hansen, T. T. 2019, *ApJ*, 870, 83, doi: [10.3847/1538-4357/aaf3bb](https://doi.org/10.3847/1538-4357/aaf3bb)
- Ji, A. P., Li, T. S., Hansen, T. T., et al. 2020, *AJ*, 160, 181, doi: [10.3847/1538-3881/abacb6](https://doi.org/10.3847/1538-3881/abacb6)
- Kelson, D. D. 2003, *PASP*, 115, 688, doi: [10.1086/375502](https://doi.org/10.1086/375502)
- Kirby, E. N., Cohen, J. G., Guhathakurta, P., et al. 2013, *ApJ*, 779, 102, doi: [10.1088/0004-637X/779/2/102](https://doi.org/10.1088/0004-637X/779/2/102)
- Kobayashi, C., Karakas, A. I., & Lugaro, M. 2020, *ApJ*, 900, 179, doi: [10.3847/1538-4357/abae65](https://doi.org/10.3847/1538-4357/abae65)
- Kobayashi, C., Mandel, I., Belczynski, K., et al. 2023, *ApJL*, 943, L12, doi: [10.3847/2041-8213/acad82](https://doi.org/10.3847/2041-8213/acad82)
- Law, D. R., & Majewski, S. R. 2010, *ApJ*, 714, 229, doi: [10.1088/0004-637X/714/1/229](https://doi.org/10.1088/0004-637X/714/1/229)
- Limberg, G., Queiroz, A. B. A., Perottoni, H. D., et al. 2023, *ApJ*, 946, 66, doi: [10.3847/1538-4357/acb694](https://doi.org/10.3847/1538-4357/acb694)
- Limberg, G., Ji, A. P., Naidu, R. P., et al. 2024, *MNRAS*, 530, 2512, doi: [10.1093/mnras/stae969](https://doi.org/10.1093/mnras/stae969)
- Lugaro, M., Karakas, A. I., Stancliffe, R. J., & Rijs, C. 2012, *ApJ*, 747, 2, doi: [10.1088/0004-637X/747/1/2](https://doi.org/10.1088/0004-637X/747/1/2)
- Maiolino, R., & Mannucci, F. 2019, *A&A Rv*, 27, 3, doi: [10.1007/s00159-018-0112-2](https://doi.org/10.1007/s00159-018-0112-2)
- Majewski, S. R., Skrutskie, M. F., Weinberg, M. D., & Ostheimer, J. C. 2003, *ApJ*, 599, 1082, doi: [10.1086/379504](https://doi.org/10.1086/379504)
- Mardini, M. K., Frebel, A., & Chiti, A. 2024, *MNRAS*, 529, L60, doi: [10.1093/mnras/sl4d197](https://doi.org/10.1093/mnras/sl4d197)
- Marshall, J. L., Hansen, T., Simon, J. D., et al. 2019, *ApJ*, 882, 177, doi: [10.3847/1538-4357/ab3653](https://doi.org/10.3847/1538-4357/ab3653)
- Martin, N. F., Starkenburg, E., Yuan, Z., et al. 2024, *A&A*, 692, A115, doi: [10.1051/0004-6361/202347633](https://doi.org/10.1051/0004-6361/202347633)
- Mateo, M. L. 1998, *ARA&A*, 36, 435, doi: [10.1146/annurev.astro.36.1.435](https://doi.org/10.1146/annurev.astro.36.1.435)
- Matsuno, T., Hirai, Y., Tarumi, Y., et al. 2021, *A&A*, 650, A110, doi: [10.1051/0004-6361/202040227](https://doi.org/10.1051/0004-6361/202040227)
- McConnachie, A. W. 2012, *AJ*, 144, 4, doi: [10.1088/0004-6256/144/1/4](https://doi.org/10.1088/0004-6256/144/1/4)
- Monty, S., Belokurov, V., Sanders, J. L., et al. 2024, *MNRAS*, 533, 2420, doi: [10.1093/mnras/stae1895](https://doi.org/10.1093/mnras/stae1895)
- Mucciarelli, A., Bellazzini, M., & Massari, D. 2021, *A&A*, 653, A90, doi: [10.1051/0004-6361/202140979](https://doi.org/10.1051/0004-6361/202140979)
- Naidu, R. P., Ji, A. P., Conroy, C., et al. 2022, *ApJL*, 926, L36, doi: [10.3847/2041-8213/ac5589](https://doi.org/10.3847/2041-8213/ac5589)
- Niederste-Ostholt, M., Belokurov, V., Evans, N. W., & Peñarrubia, J. 2010, *ApJ*, 712, 516, doi: [10.1088/0004-637X/712/1/516](https://doi.org/10.1088/0004-637X/712/1/516)
- Nomoto, K., Kobayashi, C., & Tominaga, N. 2013, *ARA&A*, 51, 457, doi: [10.1146/annurev-astro-082812-140956](https://doi.org/10.1146/annurev-astro-082812-140956)
- Odenkirchen, M., Grebel, E. K., Harbeck, D., et al. 2001, *AJ*, 122, 2538, doi: [10.1086/323715](https://doi.org/10.1086/323715)
- Oh, W. S., Nordlander, T., Da Costa, G. S., Bessell, M. S., & Mackey, A. D. 2024, *MNRAS*, 528, 1065, doi: [10.1093/mnras/stae081](https://doi.org/10.1093/mnras/stae081)
- Onken, C. A., Wolf, C., Bessell, M. S., et al. 2019, *PASA*, 36, e033, doi: [10.1017/pasa.2019.27](https://doi.org/10.1017/pasa.2019.27)
- Ou, X., Ji, A. P., Frebel, A., Naidu, R. P., & Limberg, G. 2024, *ApJ*, 974, 232, doi: [10.3847/1538-4357/ad6f9b](https://doi.org/10.3847/1538-4357/ad6f9b)
- Pace, A. B. 2024, arXiv e-prints, arXiv:2411.07424, doi: [10.48550/arXiv.2411.07424](https://doi.org/10.48550/arXiv.2411.07424)
- Placco, V. M., Frebel, A., Beers, T. C., & Stancliffe, R. J. 2014, *ApJ*, 797, 21, doi: [10.1088/0004-637X/797/1/21](https://doi.org/10.1088/0004-637X/797/1/21)
- Placco, V. M., Sneden, C., Roederer, I. U., et al. 2021, *Research Notes of the American Astronomical Society*, 5, 92, doi: [10.3847/2515-5172/abf651](https://doi.org/10.3847/2515-5172/abf651)
- Queiroz, A. B. A., Anders, F., Santiago, B. X., et al. 2018, *MNRAS*, 476, 2556, doi: [10.1093/mnras/sty330](https://doi.org/10.1093/mnras/sty330)
- Ramos, P., Antoja, T., Yuan, Z., et al. 2022, *A&A*, 666, A64, doi: [10.1051/0004-6361/202142830](https://doi.org/10.1051/0004-6361/202142830)
- Roederer, I. U., Cowan, J. J., Karakas, A. I., et al. 2010, *ApJ*, 724, 975, doi: [10.1088/0004-637X/724/2/975](https://doi.org/10.1088/0004-637X/724/2/975)
- Roederer, I. U., Hattori, K., & Valluri, M. 2018, *AJ*, 156, 179, doi: [10.3847/1538-3881/aadd9c](https://doi.org/10.3847/1538-3881/aadd9c)
- Santiago, B. X., Brauer, D. E., Anders, F., et al. 2016, *A&A*, 585, A42, doi: [10.1051/0004-6361/201323177](https://doi.org/10.1051/0004-6361/201323177)
- Schlafly, E. F., & Finkbeiner, D. P. 2011, *ApJ*, 737, 103, doi: [10.1088/0004-637X/737/2/103](https://doi.org/10.1088/0004-637X/737/2/103)
- Sestito, F., Vitali, S., Jofre, P., et al. 2024a, *A&A*, 689, A201, doi: [10.1051/0004-6361/202450553](https://doi.org/10.1051/0004-6361/202450553)
- Sestito, F., Ardern-Arentsen, A., Vitali, S., et al. 2024b, *A&A*, 690, A333, doi: [10.1051/0004-6361/202451258](https://doi.org/10.1051/0004-6361/202451258)
- Siegel, D. M., Barnes, J., & Metzger, B. D. 2019, *Nature*, 569, 241, doi: [10.1038/s41586-019-1136-0](https://doi.org/10.1038/s41586-019-1136-0)
- Simon, J. D. 2019, *ARA&A*, 57, 375, doi: [10.1146/annurev-astro-091918-104453](https://doi.org/10.1146/annurev-astro-091918-104453)
- Simon, J. D., Li, T. S., Drlica-Wagner, A., et al. 2017, *ApJ*, 838, 11, doi: [10.3847/1538-4357/aa5be7](https://doi.org/10.3847/1538-4357/aa5be7)
- Simon, J. D., Li, T. S., Erkal, D., et al. 2020, *ApJ*, 892, 137, doi: [10.3847/1538-4357/ab7ccb](https://doi.org/10.3847/1538-4357/ab7ccb)

- Skowronski, J., Boeltzig, A., Ciani, G. F., et al. 2023, *PhRvL*, 131, 162701, doi: [10.1103/PhysRevLett.131.162701](https://doi.org/10.1103/PhysRevLett.131.162701)
- Skúladóttir, Á., Hansen, C. J., Salvadori, S., & Choplin, A. 2019, *A&A*, 631, A171, doi: [10.1051/0004-6361/201936125](https://doi.org/10.1051/0004-6361/201936125)
- Skúladóttir, Á., & Salvadori, S. 2020, *A&A*, 634, L2, doi: [10.1051/0004-6361/201937293](https://doi.org/10.1051/0004-6361/201937293)
- Skúladóttir, Á., Vanni, I., Salvadori, S., & Lucchesi, R. 2024, *A&A*, 681, A44, doi: [10.1051/0004-6361/202346231](https://doi.org/10.1051/0004-6361/202346231)
- Snedden, C., Cowan, J. J., & Gallino, R. 2008, *ARA&A*, 46, 241, doi: [10.1146/annurev.astro.46.060407.145207](https://doi.org/10.1146/annurev.astro.46.060407.145207)
- Snedden, C. A. 1973, PhD thesis, The University of Texas at Austin.
- Sobeck, J. S., Kraft, R. P., Sneden, C., et al. 2011, *AJ*, 141, 175, doi: [10.1088/0004-6256/141/6/175](https://doi.org/10.1088/0004-6256/141/6/175)
- Starkenburger, E., Martin, N., Youakim, K., et al. 2017a, *MNRAS*, 471, 2587, doi: [10.1093/mnras/stx1068](https://doi.org/10.1093/mnras/stx1068)
- . 2017b, *MNRAS*, 471, 2587, doi: [10.1093/mnras/stx1068](https://doi.org/10.1093/mnras/stx1068)
- Tacconi, L. J., Genzel, R., & Sternberg, A. 2020, *ARA&A*, 58, 157, doi: [10.1146/annurev-astro-082812-141034](https://doi.org/10.1146/annurev-astro-082812-141034)
- Timmes, F. X., Woosley, S. E., & Weaver, T. A. 1995, *ApJS*, 98, 617, doi: [10.1086/192172](https://doi.org/10.1086/192172)
- Tolstoy, E., Hill, V., & Tosi, M. 2009, *ARA&A*, 47, 371, doi: [10.1146/annurev-astro-082708-101650](https://doi.org/10.1146/annurev-astro-082708-101650)
- Travaglio, C., Gallino, R., Arnone, E., et al. 2004, *ApJ*, 601, 864, doi: [10.1086/380507](https://doi.org/10.1086/380507)
- Tsujimoto, T., & Shigeyama, T. 2003, *ApJL*, 584, L87, doi: [10.1086/368403](https://doi.org/10.1086/368403)
- Umeda, H., & Nomoto, K. 2003, *Nature*, 422, 871, doi: [10.1038/nature01571](https://doi.org/10.1038/nature01571)
- Vasiliev, E., & Belokurov, V. 2020, *MNRAS*, 497, 4162, doi: [10.1093/mnras/staa2114](https://doi.org/10.1093/mnras/staa2114)
- Vitali, S., Arentsen, A., Starkenburg, E., et al. 2022, *MNRAS*, 517, 6121, doi: [10.1093/mnras/stac2869](https://doi.org/10.1093/mnras/stac2869)
- Vitali, S., Rojas-Arriagada, A., Jofré, P., et al. 2024, arXiv e-prints, arXiv:2412.06896, doi: [10.48550/arXiv.2412.06896](https://doi.org/10.48550/arXiv.2412.06896)
- Wanajo, S., Janka, H.-T., & Müller, B. 2011, *ApJL*, 726, L15, doi: [10.1088/2041-8205/726/2/L15](https://doi.org/10.1088/2041-8205/726/2/L15)
- Yong, D., Kobayashi, C., Da Costa, G. S., et al. 2021, *Nature*, 595, 223, doi: [10.1038/s41586-021-03611-2](https://doi.org/10.1038/s41586-021-03611-2)